ELSEVIER

Contents lists available at ScienceDirect

Journal of Catalysis

journal homepage: www.elsevier.com/locate/jcat



Research article

Microkinetic modelling of post-plasma catalysis to improve the conversion of dry reforming of methane in a gliding arc plasmatron

Sara Ceulemans *0, Eduardo Morais 0, Björn Loenders 0, Annemie Bogaerts *0

Research Group PLASMANT and Center of Excellence PLASMA, Department of Chemistry, University of Antwerp, Groenenborgerlaan 171, 2020 Antwerp, Belgium Electrification Institute, University of Antwerp, Olieweg 97, 2020 Antwerp, Belgium

ARTICLE INFO

Keywords:
Plasma gas conversion
Dry reforming of methane
Post-plasma catalysis
OD microkinetic model

ABSTRACT

Plasma conversion of the greenhouse gases CO_2 and CH_4 into useful products via dry reforming of methane (DRM) has shown promising results in gliding arc and other warm plasmas, but the conversions and product distribution can be further improved. In this work, we investigate the effects of adding a post-plasma Ni catalyst, to achieve extra CO_2 and CH_4 conversion via the catalytic DRM reaction. We developed a 0D microkinetic model to calculate gas-phase and surface reactions in the plasma, afterglow, and catalyst surface, which can be used to study both conversion trends, as well as the underlying reaction mechanisms. We examined a range of relevant parameters, and the results show an improvement in conversion, especially at high catalyst site density, catalyst bed gas temperature and fraction of gas converted by the plasma. At the optimal $30/70 \ CO_2/CH_4$ input gas mixture, our model predicts an increase in conversion from 25 %, to 68 % and 43 % for CO_2 and CH_4 , respectively, upon Ni catalyst addition. The pathway analysis reveals that adsorbed C atoms (C^*) play a critical role, and upon recombination with C^* into CO^* , they link the CO_2 and CH_4 conversion mechanisms, albeit a balance must be maintained to avoid C^* -poisoning. In addition, the pathway depends on the Ni facet, with most conversion taking place on Ni(110). Overall, our model demonstrates the positive effects of integrating postplasma catalysis to a warm plasma, guiding experimental work to obtain the highest possible conversions, by tuning the input conditions.

1. Introduction

Global warming and climate change are rapidly becoming a pressing problem. In the Paris Agreement of 2015, a goal was set to limit global warming to a maximum of 2 °C and preferably 1.5 °C compared to preindustrial levels [1]. However, to achieve this goal and remain under 1.5 °C, the emission of CO_2 should be reduced by 48 % and that of CH_4 by 34 % by 2030 relative to 2019 [2]. Therefore, multiple methods are being investigated to capture CO_2 and CH_4 from the atmosphere and either store or utilise these gases to create renewable chemicals and fuels. On the utilisation front, plasma exhibits advantages, since it can be fully driven by electricity from renewable energy sources, it is very flexible and can be efficiently applied at small and medium scale [3]. Plasma technologies can be used to convert various gases and gas mixtures. In this study, we investigate dry reforming of methane (DRM) (Reaction (R.1)) [3]:

$$CO_2(g) + CH_4(g) \rightarrow 2CO(g) + 2H_2(g) \qquad \Delta H^0 = 247 \, kJ \big/ mol \tag{R.1} \label{eq:R.1}$$

In this reaction, two greenhouse gases are converted simultaneously to create syngas, a mixture of CO and $\rm H_2$ which has numerous applications, such as production of liquid and gaseous fuels, chemicals and power generation [4]. As seen in Reaction (R.1), the stoichiometry of DRM with equal concentrations of $\rm CO_2$ and $\rm CH_4$ would provide a syngas ratio (H2/CO) of 1. Depending on the process, other syngas ratios (e.g., 2) are more desirable to create value-added chemicals, such as methanol, or in the Fischer-Tropsch synthesis of hydrocarbons [5,6]. Higher syngas ratios could be achieved by varying the stoichiometry of $\rm CO_2$ to $\rm CH_4$ in the DRM reaction [6]. This illustrates the broad range of possibilities and useful products that can be formed by combining the conversion of these two greenhouse gases.

DRM has already been investigated in several types of plasma reactors, such as dielectric barrier discharges (DBD) [7–14], gliding arc (GA) plasmas [15–20], radiofrequency (RF) plasmas [21,22],

E-mail addresses: sara.ceulemans@uantwerpen.be (S. Ceulemans), eduardo.morais@uantwerpen.be (E. Morais), bjorn.loenders@uantwerpen.be (B. Loenders), annemie.bogaerts@uantwerpen.be (A. Bogaerts).

^{*} Corresponding authors.

microwave (MW) plasmas [23-28], nanosecond-pulsed discharges (NPD) [29-33], corona discharges [34-36], and atmospheric pressure glow discharges (APGD) [6,37]. GA plasmas are particularly interesting because they can easily give rise to gas temperatures of 3000 K and higher [17,38-41], chiefly resulting in thermal conversion of CO2 and CH₄ [42]. In addition, they can operate at atmospheric pressure and their geometry has already been improved to allow more gas to flow through the active plasma, by evolving from a classical 2D GA reactor to a 3D gliding arc plasmatron (GAP), rotating gliding arc (RGA), dualvortex plasmatron or gliding arc tornado [18,43-45]. These reactors have already shown promising results for CO2 splitting, CH4 coupling and pyrolysis, DRM and treatment of other gas mixtures [17,18,43,44,46–59]. However, overall conversions are still limited, and research on CO₂ splitting has pointed out that little improvement can be expected from further improving the reactor design [60]. In this context, complementary solutions are being investigated to boost the conversions of CO₂ and CH₄. These include (i) quenching the hot gas stream after the plasma to avoid product recombination, (ii) placing a carbon bed after the plasma, (iii) preheating the gas before it enters the plasma reactor, (iv) injecting room-temperature gas in the plasma afterglow, i.e., dual gas injection and (v) combining plasma conversion with catalysis [49,61-76]. In this paper, we will investigate the latter.

Plasma-catalytic DRM has already been investigated in different types of reactors with very distinct plasma properties [7,9,14,33,36,49,70,71,77-87]. DBDs have been mostly used, because their low gas temperature allows the catalyst to be placed within the plasma discharge region, aiming at synergistic effects between plasma and catalyst [14,84,86,88-90]. However, synergy between catalyst and plasma is not always present [90,91]. In fact, in some cases, adding a catalyst can have a negative effect on the conversion of one or multiple gases [7,79,91]. In addition, the energy efficiency in DBD reactors is low compared to other plasmas reactors, both for CO2 conversion as well as for DRM [3]. In contrast, GA plasmas have achieved better results, but due to their higher temperatures, catalysts must be placed downstream from the plasma, in so-called post-plasma catalysis. This strategy aims to harness the heat created in the GA plasma to activate heterogeneous catalysts and further enhance the conversion by reacting leftover CO₂ and CH₄ molecules (from the plasma region) into syngas. Even though our reactor setup does not allow for in-plasma catalysis, where radical and excited species may interact with the catalyst surface, the coupling of an arc plasma reactor with downstream catalysis enables the efficient utilisation of the heat generated in the plasma region (which would otherwise be wasted) for catalyst activation. Some experiments have been carried out on post-plasma catalysis in GA reactors for DRM, with some studies showing a boost in conversion, energy efficiency and/or selectivity, while others report a decrease in conversion, depending on the position of the catalyst (i.e., distance between plasma and catalyst bed), and Ar or O2 addition [49,70-73,92,93]. However, most of this research has focussed exclusively on experiments, with limited surface modelling being carried out. While experiments can demonstrate the effect of post-plasma catalysis on metrics such as conversion and energy efficiency, they do not explain the underlying reasons of these trends. Indeed, to examine the latter aspect, modelling is required.

In this study, we investigate post-plasma catalysis for DRM in a GAP, coupled with a downstream Ni catalyst, by using a 0D microkinetic model describing the chemistry in the plasma, its afterglow and at the catalyst surface. This allows us to analyse not only potential improvements in conversion, but also the underlying reaction mechanisms, both in the gas phase and on the surface. In particular, we look at the effect of several parameters on the $\rm CO_2$ and $\rm CH_4$ conversion, namely the gas temperature in the catalyst bed, input gas mixture, catalyst site density, catalyst position after the plasma reactor, fraction of gas converted by the plasma and plasma residence time, searching for their optimal values, while elucidating the observed trends by means of the reaction mechanism. We will first explain the model, its equations and assumptions, and the reaction network utilised in the model. Next, we present

the results, which are divided in two parts: model validation by comparisons with experimental results from literature, and the results for the post-plasma catalysis of DRM in a GAP, including the mechanism analysis and different parameter variations. Finally, we end with some general conclusions.

2. Method

A 0D microkinetic model is used to investigate post-plasma catalysis using a Ni catalyst, including the chemistry in the plasma, its afterglow and at the catalyst surface. The model consists of a series of Continuously Stirred Tank Reactors (CSTRs), which are all placed next to one another. Each CSTR is calculated separately for a certain calculation time, but all CSTRs are linked because each consecutive CSTR uses the output of the previous CSTR as the input for species densities. Apart from the difference in input parameters, input species densities, and the possible presence of catalyst chemistry, all CSTRs are calculated identically, with the same underlying equations. In this section, we will first explain how one CSTR is calculated, including the mass balance and rate coefficient equations. Next, we will describe how these CSTRs are connected into the complete reactor and provide the overall reactor description. Finally, we will show how the model is used to investigate post-plasma catalysis and how we varied the different parameters.

2.1. Calculations in one CSTR

A CSTR consists of a constant volume of (in this case) gas, in which perfect mixing is assumed. This means that the concentration of a certain species remains unchanged in the entire volume and no gradients are present. Gas inflow and outflow are also included in the modelled CSTRs. In the reactor volume, the chemistry is taking place, while the inflow can be a set gas composition delivered by mass flow controllers or the output from a previous CSTR, and the outflow always has the same composition as the CSTR reactor itself. Together, the chemistry, inflow and outflow result in a mass balance equation for each species, which for the gas-phase species is given in Eq. (1) [91]:

$$\frac{\partial n_s}{\partial t} = R_{s,gas} + \frac{n_{s,in} \nu_{in}}{V_{CSTR}} - \frac{n_{s,out} \nu_{out}}{V_{CSTR}}$$
(1)

With n_s being the density of species s, t the time, $R_{s,gas}$ the net loss or formation rate of species s due to the reactions, $n_{s,in}$ and $n_{s,out}$ the density of species s of the flow into and out of the reactor, respectively, v_{in} and v_{out} the volumetric flow rate into and out of the reactor, respectively, and V_{CSTR} the volume of the CSTR reactor. This equation defines how the density of a certain species changes over time due to the chemistry taking place in the reactor (first term on the right-hand side of Eq. (1)), the inflow of species s (second term) and the outflow of species s (third term), which are the three components of a CSTR, as explained previously.

For the surface species, a coverage is used instead of a density. This coverage represents the fraction of the surface sites that is taken by a certain species and is a value between 0 and 1, with the sum of all coverages plus the fraction of free sites being equal to 1. For the surface species, a similar mass balance equation can be formulated:

$$\frac{\partial \theta_s}{\partial t} = R_{s,sturf} \tag{2}$$

With θ_s being the coverage of species s. The net loss or formation rate $R_{s,surf}$ here also includes the loss or formation of species s due to desorption or adsorption, akin to the $R_{s,gas}$ of the corresponding gasphase species. It should be noted that molecules in the gas phase and adsorbed on the surface are considered as separate species in the model. This mass balance equation is similar to Eq. (1) for gas-phase species, but does not include the terms related to inflow or outflow, as surface species will first adsorb at the surface after entering the reactor, and must

also desorb into the gas phase before they can leave the reactor. Each of the terms, chemistry, inflow and outflow, used in Eqs. (1) and (2), will be explained separately in the following subsections.

2.1.1. Chemistry

To obtain the net loss or formation rate of a species s, Eqs. (3) and (4) are applied [91]:

$$R_{s,gas} = \sum_{i.eas} \left[\left(c_{s,i}^R - c_{s,i}^L \right) r_i \right] + n_{sites} \sum_{i.eat} \left[\left(c_{s,i}^R - c_{s,i}^L \right) r_i \right]$$
(3)

$$R_{s,surf} = \sum_{i \text{ or }} \left[\left(c_{s,i}^R - c_{s,i}^L \right) r_i \right] \tag{4}$$

With $c_{s,i}^R$ and $c_{s,i}^L$ being the stoichiometric coefficient of species s in reaction i on the right (R) or left (L) hand side of the reaction equation, r_i the reaction rate of reaction i (in cm⁻³ s⁻¹ for gas-phase reactions and in s⁻¹ for surface reactions and adsorption/desorption reactions), n_{sites} the effective uniform site density of the catalyst (in cm⁻³) and the sum is taken over all gas-phase species (gas) or surface species reactions (cat), including adsorption and desorption reactions. The rate of a reaction i is calculated as $\lceil 91 \rceil$:

$$r_i = k_i \prod_{c} (a_s)^{c_{s,i}^L} \tag{5}$$

With k_i being the reaction rate coefficient of reaction i, and a_s the activity of species s. The product is taken over all reacting species s on the left side of reaction i. This activity is equal to the number density for gasphase species and equal to the coverage for surface species. For gasphase equations, k_i has units of cm³ s⁻¹ for two-body reactions and cm⁶ s⁻¹ for three-body reactions, while for surface reactions the unit of k_i is equal to s⁻¹. From this, and by comparing Eqs. (1) and (3) to Eqs. (2) and (4), there is a clear distinction between reactions in the gas phase and reactions taking place at the surface. This leads to different units, but also to different definitions of the reaction rate coefficient k_i . Therefore, the calculations of k_i and the reaction set will be explained separately for gas-phase and surface reactions.

(a) Gas-phase chemistry

The gas-phase chemistry and corresponding rate coefficients are taken from Ref. [42]. However, in this paper, we investigate a warm plasma, with gas temperatures up to 3000 K [17,38]. To simplify the model and limit the calculation times, we have reduced this chemistry set by leaving out all electron impact reactions and other reactions involving positively and negatively charged species. Indeed, at these high gas temperatures, thermal reactions are the most important, with a weighted mean absolute deviation between the concentrations for plasma conversion and thermal conversion in general lower than 0.2 %, as shown by Slaets et al. [42]. In addition, the same approximation and reduction of the gas-phase reaction networks was also made before in Ref. [74], for the same reason – thermal conversion dominates at temperatures typical of warm plasmas. This results in a reaction set for thermal DRM chemistry, containing 728 reactions.

(b) Surface chemistry

In contrast to the gas-phase chemistry, which is included in every modelled CSTR, the surface chemistry is only included in the part of the reactor where the catalyst is located. The surface chemistry is based on four facets of Ni and includes surface recombination reactions, as well as adsorption and desorption reactions. For each of these reaction types, the rate coefficients are calculated as follows [94]:

$$k_{i,surf} = \frac{k_B T_{gas}}{h} e^{\left(\frac{-\Delta G_{act}}{RT_{gas}}\right)}$$
 (6)

$$k_{i,ads} = \frac{A_{site}k_BT_{gas}}{\sqrt{2\pi mk_BT_{gas}}} e^{\left(\frac{-\Delta G_{oct}}{RT_{gas}}\right)} \times 10^6 cm^3/m^3$$
 (7)

$$k_{i,des} = \frac{k_{i,ads}}{K_{eq}} = \frac{k_{i,ads}}{\left(e^{\left(\frac{-\Delta G_{ads}}{RT_{gas}}\right)\left(\frac{p_{ref} \times 10^{-6} m^{3} / cm^{3}}{k_{B}T_{gas}}\right)^{-1}}\right)}$$
(8)

With k_i being the reaction rate coefficient of reaction i for surface recombination reactions $(k_{i,surf})$, adsorption reactions $(k_{i,ads})$ and desorption reactions ($k_{i.des}$), k_B the Boltzmann constant, T_{gas} the gas temperature, h Planck's constant, ΔG_{act} the activation Gibbs free energy of the reaction, R the gas constant, A_{site} the site surface area, m the mass of the gas species that is being adsorbed, K_{eq} the equilibrium constant between adsorption and desorption, ΔG_{ads} the reaction Gibbs free energy of the corresponding adsorption reaction, and p_{ref} the reference pressure, equal to 1 bar. All variables are expressed in SI units, and where necessary converted from m³ to cm³ to obtain the rate coefficients in the units mentioned above. Eq. (6) is based on transition state theory, while Eq. (7) is the Hertz-Knudsen equation for adsorption. In turn, Eq. (8) uses the rate coefficient for adsorption calculated in Eq. (7) and applies detailed balancing to calculate the rate coefficient of the corresponding desorption reaction. In these equations, all constants or parameters are known, except for the Gibbs free energies and the site surface areas. The latter are taken from Ref. [95], from which we also sourced the density functional theory (DFT) data. The Gibbs free energies are calculated with:

$$\Delta G_{act} = \Delta H_{act} \tag{9}$$

$$\Delta G_{ads} = \Delta H_{ads} + E_{lat} - T_{gas} \Delta S_{ads} \tag{10}$$

With ΔH_{act} being the activation enthalpy of a reaction, ΔH_{ads} the adsorption reaction enthalpy, calculated as the difference of the activation energy of adsorption and desorption, E_{lat} the lateral interaction energy and ΔS_{ads} the adsorption entropy. The lateral interaction energy requires three parameters, as further explained in Section S1.2 in the supporting information (SI). A sensitivity analysis for the lateral interaction parameters was also carried out and presented later in the SI, in Section S2.1.4. We did not include an entropy term in Eq. (9), because this would require frequency data for the surface species, which were not available in Ref. [95]. This approximation is justified, because adsorbed species typically have a low entropy value, due to losing their translational degrees of freedom upon adsorption. The entropy only contributes significantly to the Gibbs free energy when very low frequencies (below 50 cm⁻¹ for 300-500 K) are present in the vibrational modes of the surface species, because the vibrational entropy is in general smaller than translational entropy, resulting in negligible entropy differences between the adsorbed species [96]. Indeed, in previous models, the same approximation has been applied by setting the entropy values of adsorbed species to zero, and therefore including no entropy difference in Langmuir-Hinshelwood reactions [97,98]. The enthalpy values, taken from the DFT calculations in the study of Sterk et al. [95], along with all reactions included in the model, are presented in Table S1 in Section S1.1 in the SI.

Both enthalpy terms (ΔH_{act} and ΔH_{ads}) are based on the values given in Fig. 4 in Ref. [95]. In addition, we added the same destabilisation corrections mentioned in this reference, namely a destabilisation energy of 40 kJ/mol for CO* and of 20 kJ/mol for H*. As a result, all activation enthalpies for reactions that include CO* and/or H* as reactants are decreased by 40 kJ/mol and/or 20 kJ/mol, respectively. This correction is based on literature, which shows that the approach and method used in Ref. [95] for the DFT calculations gives rise to an overbinding of about 40 kJ/mol for CO*, and on the assumption that H does not adsorb on the most stable site of Ni [95,99]. In addition, we correct the adsorption enthalpy by adding some corrections to the enthalpy of the gas-phase species, based on equations in Ref. [100], which is explained further in Section S1.2 in the SI. Similarly, the entropy is also calculated from

formulas in Ref. [100], using the ideal gas limit approximation:

$$\Delta S_{ads} = -S_{gas} = -(S_{trans} + S_{rot}) \tag{11}$$

With S_{gas} being the entropy of the gas molecule that adsorbs on the catalyst, and S_{trans} and S_{rot} the translational and rotational entropy of this gas species, respectively. The equations for S_{trans} and S_{rot} , and a longer explanation on the entropy calculations and their assumptions are presented in Section S1.3 in the SI. These assumptions include disregarding the vibrational entropy contribution of the gas-phase species, which can be justified given their low contribution to the total entropy of these species, as explained in Section S1.3 in the SI.

Above, we described the equations for a general, uniform catalyst surface. However, the modelled Ni catalyst consists of four different facets, namely two terrace site facets Ni(111) and Ni(100), and two stepedge site facets Ni(110) and Ni(211). The description of these facets and an estimation of the site distribution based on the size of the Ni particles are given in Ref. [95]. In their paper, Sterk et al. calculated facet distributions based on Wulff constructions and common neighbour analysis, and found that in the upper range of the tested particle sizes (around 7 nm up to 9.5 nm), the distribution converges to (0.45, 0.15, 0.10, 0.30) for the (111, 110, 100, 211) facets, respectively. Since one of the validation papers, as well as other papers in literature, report similar or slightly higher Ni crystal sizes for DRM catalysts [14,49,70,101,102], we have adopted this converged facet distribution in our model.

To include this separation between the facets, we consider the same species adsorbed on different facets as different species. To simplify the model, we did not include any diffusion of species between the facets, as is also done in Ref. [95]. In addition, we do not account for intrafacet and interfacet diffusion, as they are marked by much lower activation barriers of diffusion compared to adsorption and desorption, making diffusion significantly faster than adsorption and desorption, especially at elevated temperatures [103–105]. As a result, diffusion equilibrium will be reached much faster than the onset of adsorption/desorption reactions, and particularly for intrafacet diffusion this has the consequence that surface reactions are kinetically limited, and not diffusion-limited, justifying the assumption to neglect them in the model.

Alongside the surface reactions that follow a Langmuir-Hinshelwood mechanism and have rate equations as defined above, we have also added two Eley-Rideal reactions to each facet, namely the Boudouard reaction and reverse Boudouard reaction. At temperatures above 1200 K, the reverse Boudouard reaction will limit the amount of carbon deposited on the surface and counteract C*-poisoning on the surface. These rate coefficients are taken from Ref. [62] and also have units of cm 3 s $^{-1}$ (see Table S1 in Section S1.1 in the SI).

(c) Combining gas-phase chemistry and surface chemistry

The gas-phase chemistry and surface chemistry are solved simultaneously in the model. However, the gas-phase reaction rates have units of cm⁻³ s⁻¹, while s⁻¹ is the unit of surface reaction rates, as defined by the equations above. To create a uniform set that can be used in the differential equations, the units of surface reaction rates must be converted into cm⁻³ s⁻¹ using the effective uniform surface site density in cm⁻³. This effective uniform site density accounts for the assumption of our model that all sites are equally accessible for the gas-phase species. More specifically, the effects of catalyst dispersion, particle size, exposed surface area and other properties related to transport of the gas-phase species to and from the catalytic sites, are all included in this parameter. In other words, we assume that the catalytic reactions are kinetically limited, and not limited by transport, since transport in the gasphase itself cannot be accounted for in a 0D model. In addition, as mentioned above, this effective uniform site density was calculated per unit of gas volume, in order to have an effective conversion factor between gas-phase and surface reaction rates. Hereafter, we will refer to this effective uniform surface site density of the catalyst simply as the site density. The chosen default surface site density used in this study is equal to 10^{19} cm $^{-3}$, which is in line with other reports for Ni catalysts in literature [106]. Moreover, to assess the effect of site density, we will vary this parameter (from 10^{16} to 10^{20} cm $^{-3}$) and study its impact on the results, as explained in Section S1.6.1.

2.1.2. Inflow

The definition of the inflow depends on the CSTR that is being calculated. For the first CSTR, the inflow is a constant value, equal to the flow rate that flows into the reactor. For our research, we assumed a flow rate of 10 $L_{\rm n}/{\rm min}$ (273.15 K and 1 atm), which is the flow rate used in the GAP experiments in Ref. [62], from which the temperature profiles were sourced (see Section 2.2.2). In subsequent CSTRs, the inflow corresponds to the output of the previous CSTR. This means that this inflow rate can vary over time.

2.1.3. Outflow

The value of the outflow rate is based on the condition that a constant pressure is maintained in the reactor. Because the inflow rate is a set value, and the chemistry will result in an increase or decrease of the number of species, the outflow rate is defined such that the total pressure p_{tot} in the reactor remains constant. This is done by applying the following formula [91]:

$$v_{out} = v_{in} + \frac{V_{CSTR} \sum_{s,gas} R_{s,gas}}{\sum_{s,gas} n_s} = v_{in} + \frac{V_{CSTR} k_b T_{gas}}{p_{tot}} \sum_{s,gas} R_{s,gas}$$
(12)

 $R_{s,gas}$ in this case includes all gas-phase reactions and the adsorption and desorption reactions, and has a positive value when the total number density increases due to the chemistry in the reactor. By this definition of the outflow rate, the gas expansion expected in DRM is effectively accounted for (see Reaction (R.1) in the Introduction).

2.1.4. Solving the mass balance equation

The objective of the calculations in one CSTR is to determine the densities and coverages of all species. Therefore, for each species *s* a mass balance equation (Eqs. (1) and (2)) is set up, which represents the change in density or coverage of that species over time, and which together create a set of differential equations. Through the different reactions in the chemistry set, these differential equations depend on each other, and therefore they are solved together using the Python differential equation solver "solve_ivp" in the scipy.integrate module. More detailed solver settings can be found in Section S1.4 in the SI. The output generated from this model is the variation of the densities, coverages, outflow rate and reaction rates over time.

2.2. Reactor description

2.2.1. Validation simulations

The model was extensively validated against two independent sets of experimental data, presented in Ref. [14] and Ref. [106], and referred to as "Paper 1" and "Paper 2", respectively. In Paper 1, experiments for both thermal and plasma catalysis in a DBD were carried out, for CO2 combined with either CH₄ or C₂H₆, in order to prove the presence of plasma-catalyst interactions. We compared our simulations to the conversion and yield results from thermal catalysis for DRM shown in this paper. In Paper 2, on the other hand, only thermal catalysis experiments were carried out and combined with a model. The authors applied multiple gas mixtures, including DRM, steam reforming of methane (SRM, $CH_4 + H_2O$ to $CO + H_2$) and DRM with the addition of H_2 or H_2O , all of which we could use as comparison. Only oxidative reforming of CH₄ was not useful for us, as our model does not contain O₂. Indeed, while CO_2 splitting leads to O_2 formation, this is not the case in DRM, where the O atoms from CO2 splitting rather react with H atoms into H₂O than into O₂ [107,108]. We used this paper to validate our model by comparing the concentrations with the experiments. More details on how the validation was carried out are presented in Section S1.5 of the

SI, while the results are presented in Section 3.1.

2.2.2. GAP simulations

After validation, the model is used to investigate post-plasma catalysis by combining a GAP reactor with a Ni catalyst in the afterglow. For these simulations, multiple CSTRs are calculated in series, connecting the gas-phase reactions in the plasma region to the afterglow and the catalyst bed, where both gas-phase and surface reactions take place. A schematic overview of the modelled reactor is given in Fig. 1a, which indicates the three different parts of the reactor (plasma, afterglow without catalyst and afterglow with catalyst), the boundaries between the CSTRs and the dimensions. Each of these parts will be explained separately below.

(a) Plasma

The plasma consists of one CSTR with a constant temperature of 3000 K. Indeed, while a gliding arc plasma is spatially and temporally non-uniform, in our 0D model we adopted one temperature for the plasma, which represents an effective average of the arc gas temperature. This plasma temperature is estimated from typical gas temperatures for GA reactors [17,38–41]. As can be seen in Fig. 1a, we do not define a fixed length of the plasma part of the reactor, in contrast to the afterglow and the catalyst. Instead, we define a residence time, which can be converted into a length as follows:

$$v_{in}t = V = \pi r^2 L \Rightarrow L = \frac{v_{in}t}{\pi r^2}$$
 (13)

With v_{in} being the volumetric flow rate into the reactor (cm³ s⁻¹, converted to mm³ s⁻¹), t the residence time (s), V the volume of the plasma CSTR (cm³, converted to mm³), r the radius of the plasma reactor, in our case 15 mm, and L the length of the plasma CSTR (mm). This residence time can then be varied for different simulations, between 0.01 ms and 100 ms, as explained in Section S1.6.6. The default value is 1 ms, which we estimated from previous research into GA reactors and their reactor dimensions [60,109,110]. Using this residence time and gas temperature, almost all input gas will be converted to the thermodynamically

most stable products. However, the literature overview plot in Ref. [3] and Ref. [6], which relates the conversion and energy cost results of DRM in different reactors, shows that the conversion in GA reactors ranges between 5 % and 50 %. This can be caused by the limited fraction of gas passing through the plasma and unwanted back-reactions, which cannot entirely be captured by the model, for two reasons: (i) our model considers a stepwise temperature drop in the afterglow (see below) instead of a continuous one, and (ii) 0D models make certain assumptions and approximations, in particular perfect mixing. Therefore, to account for this effect, we limited the fraction of gas converted by the plasma to a default value of 25 %, with variations between 5 % and 45 % being investigated in this work. This accounts for the limited fraction of gas passing through the plasma arc, as well as for the fraction that is formed again by back-reactions of the products post-plasma. So, from this point onwards, we will refer to the "plasma fraction" as the amount of gas that can be converted by the plasma, including the effect of backreactions. The rest of the gas is assumed to be unconverted CO2 and CH4 with the same composition as at the inlet, as shown in Fig. 1a. Including this plasma fraction is a practical approximation in our model, needed to capture conversion changes at conditions where full conversion in the plasma is not reached. It only corresponds to the effective net conversion in the plasma when full conversion is achieved. In addition, it allows us to calculate the densities of species flowing into the afterglow and catalyst bed without assuming chemical equilibrium conditions. Due to the uncertain nature of this parameter, and to evaluate the effects of our assumption, we carried out a parameter study for the plasma fraction. The inflow rate is equal to a constant value of 10 L_n/min, taken from Ref. [62].

(b) Afterglow

We simulate a part of the afterglow without catalyst, which is used to cool the hot gas before it arrives at the catalyst. Because each CSTR is calculated with a constant temperature, this part of the reactor is divided into five CSTRs with progressively lower temperature, each having a length of 1 mm and radius of 15 mm. The temperatures are taken from a post-plasma profile measured in a GAP reactor for pure CO₂ [62], which

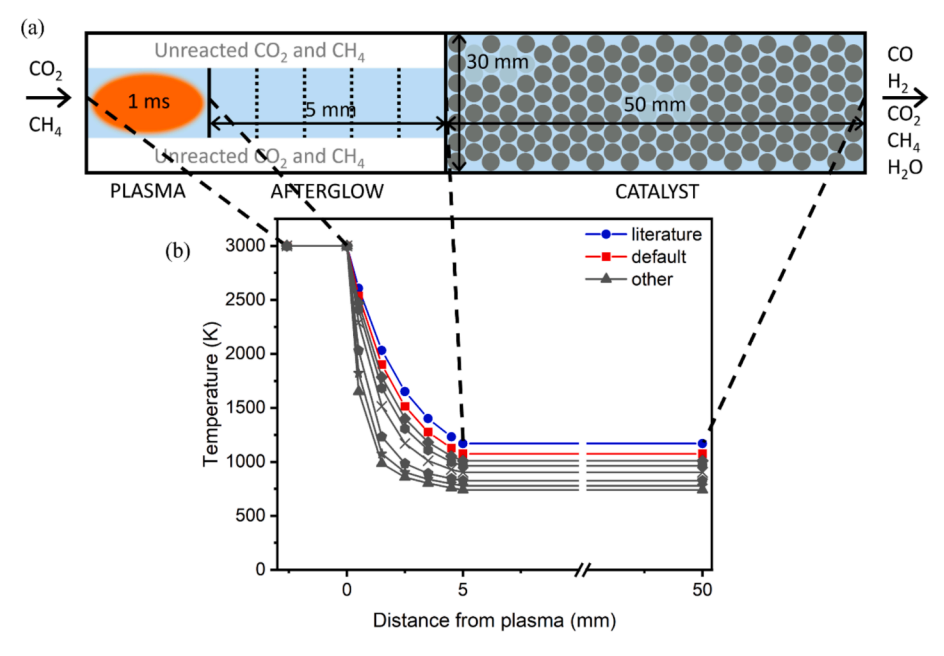


Fig. 1. (a) Schematic drawing of the reactor with indication of the plasma, afterglow and catalyst bed. The 3D reactor cylinder that is simulated is drawn as a 2D reactangle, with the dimensions indicated, but not in scale to retain clarity in the figure. The light blue background indicates the parts where the gas-phase chemistry is solved, while the grey spheres correspond to surface chemistry. "Unreacted CO₂ and CH₄" represents the fraction of gas that does not pass through the plasma arc in the centre of the reactor (see text). (b) Temperature profile through the plasma, afterglow and catalyst bed. While the temperature is constant in the plasma and catalyst bed, it decreases in the afterglow with the solid datapoints corresponding to the temperature in each afterglow CSTR. We adopt different temperature profiles in the afterglow to study the effect of temperature in the catalyst bed (see text). (For interpretation of the references to colour in this figure legend, the reader is referred to the web version of this article.)

is shown in blue circles ("literature") in Fig. 1b. The assumption of 25 % plasma fraction is also applied here. Indeed, we assume no mixing between the unconverted and reacting $\rm CO_2$ and $\rm CH_4$ molecules in the afterglow.

(c) Catalyst bed

In contrast to the plasma and afterglow, the catalyst bed will cause the gas flow to spread out radially at the catalyst, and more mixing will take place. Therefore, we assume that the converted gas (with a default fraction of 25 %) and the unconverted gas (with a default fraction of 75 %) are perfectly mixed across the entire bed. This also includes the assumption of axial mixing, and therefore the catalyst is calculated as one CSTR, like the plasma. The default temperature in the catalyst CSTR is equal to 1075 K at 5 mm (red squares in Fig. 1b). However, we vary this temperature by adopting different temperature profiles in the afterglow, as shown in Fig. 1b. Details on how the default temperature profile is obtained from the temperature profile in Ref. [62] are explained in Section S1.6 in the SI, where all parameter variations are explained in more detail. This constant temperature in the complete catalyst bed is assumed for simplicity but could be achieved experimentally by adding a heat insulating jacket around the catalyst part of the reactor. While the radius is kept at 15 mm, the length of the catalyst bed is equal to 50 mm, which is in the same order of magnitude as the length of typical thermal catalyst beds and post-plasma carbon beds used previously in experiments [14,62,76,106].

2.3. Parameter variation and result evaluation

The model described above is used to investigate the effect of six different parameters on the calculated CO2 and CH4 conversion and product distribution. These parameters are summarised in this section, as well as the equations to analyse the results. First, we vary the site density, between 10^{16} cm⁻³ and 10^{20} cm⁻³ (default 10^{19} cm⁻³), probing the effect of the surface reactions on the overall results. Second, we change the temperature profile as shown in Fig. 1b, to obtain varying gas temperatures in the catalyst bed between 741 K and 1170 K (default 1075 K). Third, we test different "plasma fractions" (see definition in section 2.2.2 above) between 5 % and 45 % in steps of 10 %pt. (default 25 %). Fourth, the input gas mixture is varied, using CO₂ fractions of 10, 20, 30, 50, 70 and 90 % (default 50 %). Besides these four parameter variations, we also discuss two extra parameters, namely the position of the catalyst bed and the residence time in the plasma, but these are reported in Sections S2.2.1 and S2.2.2, respectively, in the SI, as catalyst bed positions have a similar effect as the temperature variation and residence times do not show a large influence on the results. Further details on the selection of these parameters can be found in Section S1.6 in the SI.

All simulations are calculated until steady state, in which the densities and rates do not vary more than 0.1 % over the last half of the calculated time (usually 10,000 s) for the GAP simulations, and the compared metrics no longer visibly change for the validation results (after 3600 s). To investigate the effect of the catalyst, two simulations are carried out for each setting: one simulation is calculated as described above, and another, with the exact same settings but without any surface chemistry reactions. By comparing the results from both simulations, the effect of the catalyst can be isolated.

Besides the direct output from the simulations themselves, such as the densities, coverages and reaction rates, we also use this output to calculate the conversion of ${\rm CO_2}$ and ${\rm CH_4}$. This conversion is calculated as follows:

$$\chi = \frac{y_{in} - \alpha y_{out}}{y_{in}} \times 100\% \tag{14}$$

With χ being the conversion (in %), y_{in} and y_{out} the input and output molar gas fraction of the species, respectively, and α the flux ratio. The input gas fraction is a constant setting, which depends on the input gas

mixture, and the output fraction is calculated as the ratio of the density of the species at the end of the catalyst bed over the total density, considering only the gas-phase species. The flux ratio is included to take gas expansion into account (inherent to the DRM reaction, see Reaction (R.1) in the Introduction) and is defined as the ratio of the outflow rate over the inflow rate. In this case, it is calculated using the atom balance as explained in Ref. [111], which leads to the formula:

$$\alpha = \frac{\sum\limits_{s} \mu_{s}^{A} y_{s}^{is}}{\sum\limits_{s} \mu_{s}^{A} y_{s}^{out}}$$
 (15)

With μ_s^A being the number of A atoms in species s and y_s^{in} and y_s^{out} the input and output molar fraction of species s, respectively, which can be obtained from the initial conditions and the output densities. To calculate α based on the atom balance, we do not consider the surface species, only the gas-phase species, because the influence of the surface coverages on the flux ratio is negligible. However, when C*-poisoning occurs at the surface, the flux ratio calculated using the C-balance starts to deviate from the flux ratio based on O or H. Therefore, we calculate the flux ratio as the average of the flux ratios based on O and H, whose values are close/equal.

Other metrics plotted in Section 3.2 or the SI are the contributions of the four different Ni catalyst facets (Eq. (16)), the obtained syngas ratio (Eq. (17)) and the product selectivity (Eq. (18), [111]):

$$C_{COf} = \frac{r_{CO \, desf}}{\sum_{f} r_{CO \, desf}} \times 100\% \tag{16}$$

With $C_{CO,f}$ being the contribution to CO production of facet f, $r_{CO,des,f}$ the net desorption rate of CO on facet f, and the sum being taken over all facets f of the surface. A similar equation is used to calculate the facet contributions to H_2 production.

$$syngas ratio = \frac{y_{02}^{out}}{y_{02}^{out}}$$
 (17)

With $y_{H_2}^{out}$ and y_{CO}^{out} being the molar fraction of H_2 and CO at the end of the reactor, respectively.

$$S_s^A = \frac{\mu_s^A \alpha y_s^{out}}{\sum_s \mu_s^A (y_s^{in} - \alpha y_s^{out})} \times 100\%$$
 (18)

With S_s^A being the selectivity of species s with respect to atom A, and the other variables are explained under Eq. (15) above. The selectivity can be calculated with respect to C, H or O in our model.

In addition to the metrics used to evaluate the performance of postplasma catalysis with the GAP reactor, some other equations are used to describe the results obtained for validation of the model. More specifically, the conversions in Paper 1 are calculated using Eq. (14) defined above, and the yield using Eq. (S5) in the SI of Ref. [14]. In Paper 2, the concentrations are calculated based on the flow rates, not the molar gas fractions or densities, in order to take gas expansion into account.

3. Results and discussion

3.1. Model validation

3.1.1. Paper 1

Before we present the GAP post-plasma catalysis results, our surface chemistry set and microkinetic model are validated against experimental data from two different papers, as explained above. The comparison results between modelled and experimental CH_4 conversion and CH_2 yield in Paper 1 [14] are given in Fig. 2, while similar results for CO_2 conversion and CO_3 yield are presented in Fig. S1 in the SI.

Upon comparison, we see that experiment and model show similar

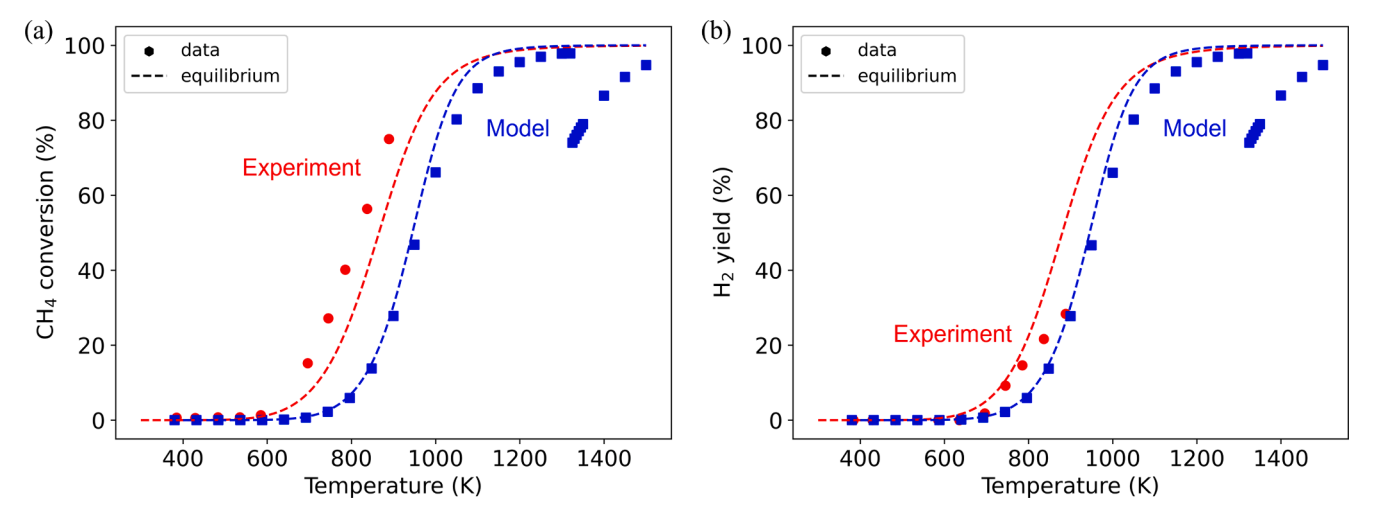


Fig. 2. (a) CH_4 conversion and (b) H_2 yield as a function of temperature for the experiments in Ref. [14] (red circles), the modelling results (blue squares) and the corresponding chemical equilibrium values for the experiments and modelling results (red and blue dashed lines, respectively). A finer temperature interval of 5 K is used around the transition point between 1300 K and 1350 K to rule out numerical artefacts in the model. (For interpretation of the references to colour in this figure legend, the reader is referred to the web version of this article.)

trends, but that the increase in CH_4 conversion and H_2 yield begins at higher temperatures in the model (740 K compared to 590 K for the onset of CH_4 conversion). The explanation for this shift can be found in the DFT-calculated enthalpies used in the model. When calculating the overall reaction enthalpy for DRM (Reaction (R.1) in the Introduction), we find 357.8 kJ/mol for all facets. However, the theoretical enthalpy for DRM is equal to 296.9 kJ/mol [112], recalculated to 0 K and without enthalpy corrections (explained in S1.2 in the SI) in order to match these to the DFT-calculated enthalpies, which is 60.9 kJ/mol lower than the enthalpy obtained from the DFT data. In addition, when carrying out the same analysis for the SRM reaction, we find a theoretical value of 267.1 kJ/mol, while the DFT-calculated value is equal to 275.7 kJ/mol, resulting in a difference of 8.6 kJ/mol.

Although we cannot address this discrepancy because we did not perform the DFT calculations ourselves, it does affect our results, as can be seen in Fig. 2, where the chemical equilibrium data shown in dashed lines are calculated based on the theoretical enthalpies (red curve) and the shifted reaction enthalpies (blue curve). These calculations were performed according to Ref. [113], for the five gas-phase species CO₂, CH₄, CO, H₂ and H₂O, where we replaced the Gibbs free energy of formation (calculated as explained in that reference for the theoretical enthalpy), by a Gibbs free energy of formation calculated from the DFT surface enthalpies and corrected as in Eq. (10) (without the lateral interaction term). Our simulation results clearly follow the shifted chemical equilibrium data as expected, while the experimental values follow the theoretical chemical equilibrium composition. A similar behaviour is observed for the CO2 conversion and CO yield, as presented in Fig. S1 in the SI. It should be noted that, as well as the deviation in the reaction enthalpy of DRM (and other reactions), the computational errors associated with the DFT calculations can also influence the results. However, we expect this to have a lesser impact compared to the shifted enthalpies. Moreover, alongside other assumptions made in 0D models, this might affect the absolute values in our results, but the overall trends will remain unaltered, as proven by these validation simulations.

While we already observe carbon deposition on two of the four facets in these simulations at temperatures from 700 K (where the conversion starts to take place) up to 1320 K, the sharp drop in conversion and yield at 1325 K can be ascribed to C*-poisoning on all facets, with the subsequent rise in conversion and yield caused by a surge in the reverse Boudouard reaction, which will be explained below. Indeed, on Ni(111) and especially Ni(110), the C* coverage strongly rises between 1320 K and 1325 K. Because Ni(111) is the most abundant facet, and Ni(110) is usually the most active facet (as will be shown in the GAP result analysis

in Section 3.2), this significantly affects the conversions and yields. Simulations with a smaller temperature interval of 5 K were included between 1300 K and 1350 K to rule out the influence of numerical artefacts, demonstrating that even in this smaller temperature interval the steep change in the metrics is still present. The sudden change in the metrics can be explained by the fact that a small change in the net C* formation between these two temperatures can lead to a large change in C* coverage on the timescale of the model. To confirm this, we analysed the dynamics of C* coverage on the Ni facets in Fig. S5a, showing that the steep decrease in conversion and yields is indeed connected to a steep increase in the C* coverage, which in turn is caused by a steep drop in the main C* consuming reaction rate (C* oxidation to CO*). More details can be found in Section S2.1.2(b) of the SI. The model shows that C*-poisoning is caused by the decomposition reaction of CH₄ into C* and H₂, rather than the Boudouard reaction between 2 CO molecules into C* and CO2, because the rate of the former increases with rising temperature, while the opposite is true for the Boudouard reaction. A more elaborate explanation for this is given in the SI (see Section S2.1.1). However, as mentioned above and is clear from Fig. 2, the conversion and yield increase again above 1325 K. This is caused by the Eley-Ridealtype (ER-type) reverse Boudouard reaction present in the surface reaction set for every facet, whereby surface C* reacts with gas-phase CO2 into gaseous CO and adsorbed CO*. Unfortunately, it is impossible to compare these predictions to experiments, because no experimental results are available at these high temperatures. Based on validation with Paper 1 for the temperatures where comparisons are possible, we can conclude that overall the surface chemistry set is robust, yielding the same trends as the experiments, with only a shift towards higher temperature, due to the reaction enthalpies in the DFT data, as explained above.

3.1.2. Paper 2

Paper 2 [106] is used for further validation and comparison with our modelling results, which is especially useful because it contains different gas mixtures that can be tested in the model. We focus here on the results for DRM, as $\rm CO_2 + CH_4$ is the gas mixture under study in this paper. The other gas mixtures (CH₄ + H₂O, CO₂ + CH₄ + H₂ and CO₂ + CH₄ + H₂O) are discussed in Section S2.1.2 in the SI.

In Fig. 3, we compare our calculated CH_4 and H_2O concentrations with the experimental ones [106] as a function of temperature, while the concentrations of the other species are presented in Fig. S3 in the SI. Akin to the comparison with Paper 1, Fig. 3a shows that the drop in CH_4 concentration (analogous to the increase in CH_4 conversion, see Fig. 2a)

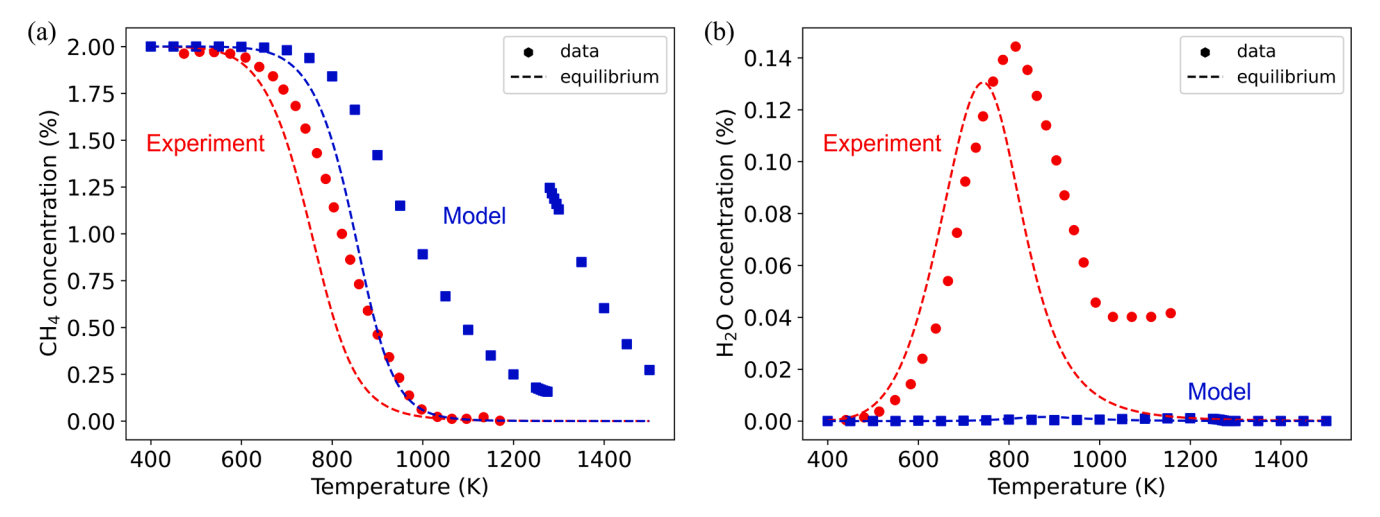


Fig. 3. (a) CH_4 and (b) H_2O concentration as a function of temperature for the experiments in Ref. [106] (red circles), the modelling results (blue squares) and the corresponding chemical equilibrium compositions for the experiments and modelling results (red and blue dashed lines, respectively). A finer temperature interval of 5 K is used around the transition point between 1250 K and 1300 K to rule out numerical artefacts in the model. (For interpretation of the references to colour in this figure legend, the reader is referred to the web version of this article.)

is shifted to higher temperatures (onset of decrease in CH_4 concentration at 770 K, instead of 630 K), due to the deviation in the model's reaction enthalpy for DRM compared to the theoretical reaction enthalpy. In addition, at around 1275 K, C^* begins to cover the surface which leads to a sharp rise in CH_4 concentrations, i.e., lowered conversion. This is again caused by C^* -poisoning on Ni(111) and Ni(110), with the subsequent drop in CH_4 concentration due to the reverse Boudouard reaction, as explained in the previous section and presented in more detail in Section S2.1.2(b) in the SI. The steep change in concentrations is narrowed to a temperature interval of 5 K, between 1275 K and 1280 K, to rule out numerical artefacts in this region of sharp transitions.

At lower temperatures, between around 600 K and 850 K, minor discrepancies are observed between modelled and experimental data and their corresponding chemical equilibrium, which strengthens confidence in our model in this temperature range. However, above 850 K, the discrepancies become more pronounced, as the calculated CH₄ concentration has a slower decrease with temperature compared to the experimental data. This is again likely due to C* formation, which is not included in the calculation of the chemical equilibrium composition. Although no clear C*-poisoning on all facets is observed between 750 K (start of the drop in CH₄ concentration) and 1275 K, some C* is formed on Ni(111) above 1000 K, and C* formation would also be increasingly favoured thermodynamically through CH₄ decomposition with rising temperature (see Fig. S4).

A key divergence between the experiments and model can be seen in Fig. 3b. In the experiments, some H₂O is formed, with a peak concentration registered about 70 K higher than the maximum in the corresponding chemical equilibrium composition value (at 815 K and 743 K, respectively). However, no H₂O is observed in our simulations or in the corresponding chemical equilibrium composition curves in the tested temperature range (see blue datapoints and dashed line). This discrepancy between the experiments and modelling data, also reflected in the chemical equilibrium data, may result in an underestimated output fraction of H₂O in our later GAP simulations. Again, this could be related to the shift in reaction enthalpy for DRM and other reactions. However, through a consistency verification of the DFT enthalpy data, which is explained in detail in the SI (see Section S2.1.2), the surface reaction enthalpies were deemed correct. Therefore, we believe that the shift in chemical equilibrium composition and absence of H₂O in the model may be caused by the adsorption and desorption reaction enthalpies. To investigate this in more detail, we carried out a literature study and sensitivity analysis on these energies, which is discussed in the next section.

3.1.3. Sensitivity analysis

To determine the effect of deviating adsorption and desorption enthalpies, we performed a sensitivity analysis, comparing the values from Ref. [95] to other DFT calculation results in literature. An overview of the collected data is presented in the supplementary Excel document provided. To define the adsorption and desorption rates, we use the activation and reaction Gibbs free energies (and therefore enthalpies) of the adsorption reaction (see Eqs. (7) and (8)). Therefore, for each species, we divided the energies available from literature into a high, mid or low energy range, and replaced the values from Ref. [95] in our surface reaction network by these high, mid and low values in two ways: (i) for all species separately, or (ii) for all species at the same time. For each new set of energies, we performed a simulation, with the same settings described in Paper 2 at 1000 K, and analysed the ensuing effect on the concentration of the different species. This is illustrated for all five gasphase species in Fig. S9. A more detailed explanation of the method for this sensitivity analysis is given in Section S2.1.3 in the SI.

Fig. S9 a, c, e, g and i illustrate the influence of every energy set on the concentration of the five gas-phase species, effectively summarising all simulations that have been carried out. From these graphs (especially Fig. S9i), it is clear that $\rm H_2O$ formation is observed for some combinations of energy values. While we expected this to be primarily related to the adsorption activation barrier and reaction energy of $\rm H_2O$ itself, this plot shows that the energies for $\rm H_2$ adsorption have the largest influence on the predicted $\rm H_2O$ concentration, and also on some of the other concentrations. Thus, the $\rm H_2$ energies are most likely causing the deviations in the chemical equilibrium composition.

Since the variation in energy sets in Fig. S9 a, c, e, g and i in the SI shows that H₂O can be formed with other reported enthalpy values, we also investigated the concentration of H₂O as a function of temperature for one of these chemistry sets, yielding a graph similar to that presented in Fig. 3b. We used the energy set "Mid Er" (see the SI-files for more information on these energy sets), containing mid, average values for all energies. The resulting plot is shown in Fig. 4, indicating the presence of H₂O, although the maximum is again shifted to higher temperatures compared to the experiments. The difference between the maximum H₂O concentration observed in the model and predicted by its chemical equilibrium value can be explained by the fact that, by collecting energies from different papers, the chemistry set becomes inconsistent, i.e., the DFT calculations behind these energies have different calculation settings, methodologies and reference values. This results in a variation in DRM reaction enthalpies on the four facets. As a consequence, the chemical equilibrium value calculation, which requires one overall

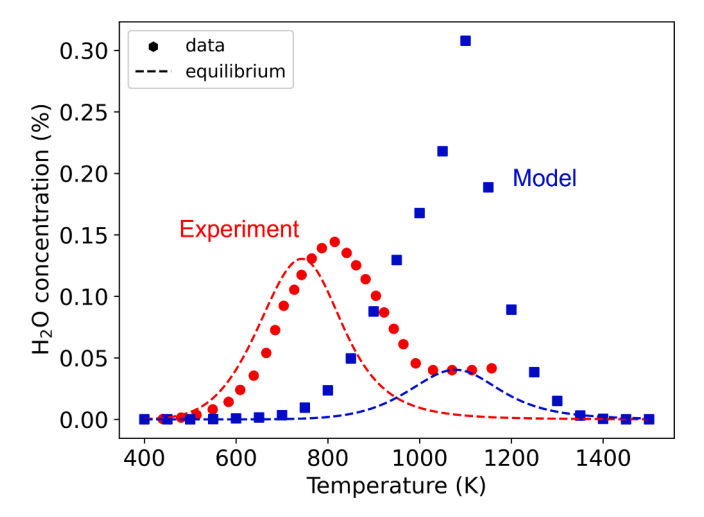


Fig. 4. H_2O concentration as a function of temperature, calculated for the energy set "Mid_Er" (blue squares), in comparison to the experiments in Ref. [106] (red circles), and the corresponding chemical equilibrium compositions for the experiments and modelling results (red and blue dashed lines, respectively). The energy values used in this set are listed in the supplementary Excel file, and a more detailed explanation is given in Section S2.1.3 in the SI. (For interpretation of the references to colour in this figure legend, the reader is referred to the web version of this article.)

reaction enthalpy, gets less reliable. However, the main objective of this figure is to show the presence of a peak in $\rm H_2O$ formation, which can clearly be observed. The plots for the other concentrations and the corresponding discussion and general conclusions can be found in Section S2.1.3 in the SI.

Together, Fig. 4 and the other figures in Section S2.1.3 in the SI show that we can reach different (perhaps more realistic) product gas mixtures, including $\rm H_2O$, when using the mid-value energy set as input enthalpies. However, adopting this energy set would lead to a larger deviation from the theoretical reaction enthalpy for DRM (454 kJ/mol compared to the theoretical value of 296.9 kJ/mol and the value of 357.8 kJ/mol from the energies of Sterk et al.)[112]. The influence that such a change would have on the chemical equilibrium composition is shown in Fig. S10 for the molar fractions of CH₄, $\rm H_2$ and $\rm H_2O$, which illustrates the even larger deviations in the chemical equilibrium composition compared to the theoretical values and the data from Sterk et al. [95,112]. Finally, since applying the new energy sets tested in the sensitivity analysis would cause inconsistencies, we decided to retain the DFT data provided by Sterk et al. in our model [95].

3.1.4. Summary

In this part we validated our surface reaction set and input enthalpies by comparing our modelled results to two independent sets of experimental data. Even though the experimental and calculated results do not always match, our model was able to capture the relevant trends observed in the experiments. In addition, the discrepancies were identified, explained and addressed. The major deviation source was the higher DFT-calculated reaction enthalpies compared to the theoretical reaction enthalpy of DRM, and other reactions such as SRM. This results in a shift in conversion to higher temperatures, and an underestimation in the amount of H₂O in the gas mixture. Additionally, by performing a sensitivity analysis, we have determined the effect of this deviation on the abnormally low H2O concentrations seen in the model, and also on the concentrations of the other gas species. Despite these issues, we decided to apply this energy set in our model, because the data from Sterk et al. provide an extensive, consistent chemistry set for DRM on Ni on four different facets. With this reaction network and energy set, we have simulated GAP post-plasma catalysis, keeping in mind the temperature shift in conversion, underestimation of H₂O and the C*- poisoning taking place at higher temperatures, as revealed by our validation efforts.

3.2. GAP results

For the GAP simulations, we have two main goals, namely to discover the reaction mechanism, and to elucidate which input conditions can lead to an improved CO_2 and CH_4 conversion and product distribution. The former goal is reached by analysing in more detail the most important route from CO_2 and CH_4 into CO and H_2 , and possible important side reactions. For the latter, we vary six different parameters. As explained in Section 2.3 above, two of these parameters, i.e., position of the catalyst bed and plasma residence time, are found to be less significant, and are therefore described in Sections S2.2.1 and S2.2.2 of the SI. The other four parameters are discussed in detail: the catalyst site density, gas temperature in the catalyst bed, fraction of gas that can be converted by the plasma, including the effect of back-reactions (simply called "plasma fraction") and input gas mixture.

3.2.1. Reaction mechanism

We first introduce the reaction mechanism, as it will be used to explain the graphs below in the parameter variations. Besides the goal of investigating the effect of post-plasma catalysis on the $\rm CO_2$ and $\rm CH_4$ conversion and product distribution, the model is especially useful to analyse the underlying reaction pathways at the catalyst surface. This analysis results in the reaction mechanism shown in Fig. 5, where the default conditions for all parameters are applied (site density of $\rm 10^{19}$ cm $^{-3}$, gas temperature in the catalyst bed of 1075 K, plasma fraction of 0.25, input gas mixture equal to 50/50 $\rm CO_2/CH_4$, position of the catalyst after the plasma of 5 mm and plasma residence time equal to 1 ms). In addition, it should be noted that only surface reactions are shown in Fig. 5, because these reactions are more important than gas-phase reactions, which become negligible in the (active) catalyst bed.

It is clear from Fig. 5 that CO2 is converted by adsorbing on the surface (as CO2*) and subsequently losing O* to form CO*, while CH4 dissociatively adsorbs on the surface (as CH3*) and sequentially dehydrogenates to C*. This C* combines with surface O* from CO2* dissociation to form CO*, which desorbs into the gas phase as CO. Hence, the formed CO does not only originate from CO2 splitting, but also from CH₄ dehydrogenation. The H* species from the dehydrogenation reactions recombine to form gas-phase H2. Besides this principal pathway, some side reactions can also take place. An example is the formation of CHO*: 8 % of the CH* does not undergo dehydrogenation to C*, but oxidises to CHO*, before losing its last H* to form CO*. As can be seen by the colours of the arrows, the formation of CHO* is the preferred route on Ni(111), while Ni(110) follows both mechanisms, though higher rates are observed via the C* pathway. This has been previously reported in literature [114-116]. Wang et al. have only investigated Ni(111) using DFT calculations, and indeed reported a preference for CHO* formation compared to C* formation [114]. On the other hand, Vogt et al. published experimental results showing that the direct carbide pathway via C* is favourable [115]. As Ni(110) is more active than Ni(111) in our model and mostly reacts through C*, our model supports these experimental results. In addition, Fan et al., whose work includes Ni(111), Ni(100) and Ni(211), calculated the relative contribution of the different pathways, and found a higher contribution of C* to CO formation, with CHO* formation as the second most important pathway, again consistent with our results, although Ni(110) was not taken into account in their work [116]. These validations boost the confidence in our model. Besides CHO* formation, another side reaction pathway observed in Fig. 5 is the conversion of H₂O created in the plasma. When H₂O is present in the gas mixture (which is the case at the highest plasma fractions, and at some of the input gas mixture ratios, as presented in the next section), this H₂O can adsorb on the surface, consecutively lose both of its hydrogen atoms and create O* on the surface. The H^{\star} will recombine to form H_2 , while the O^{\star} can be used

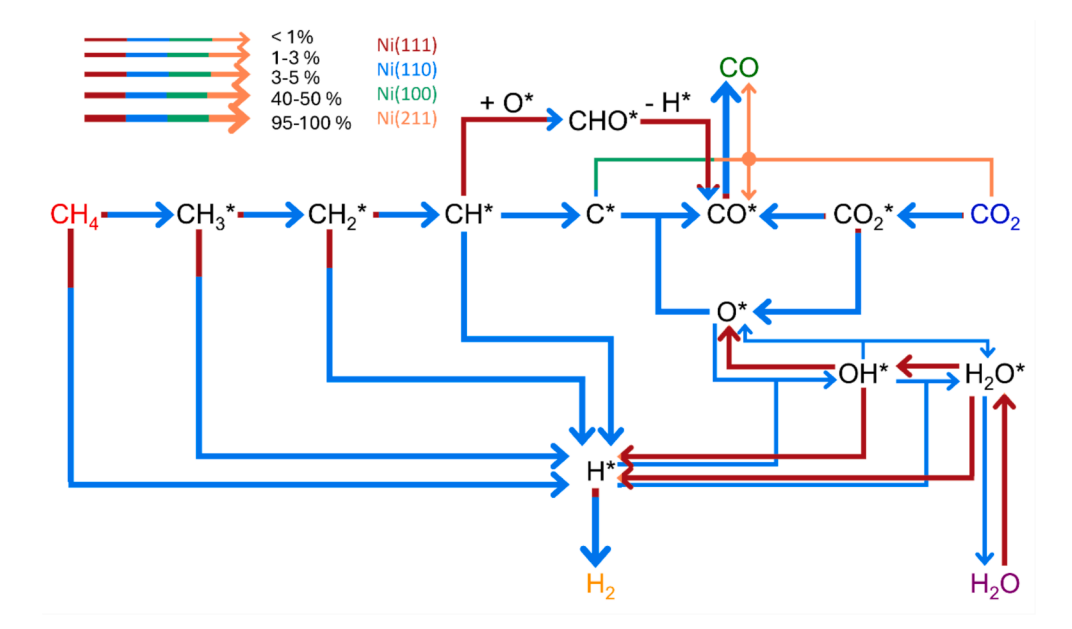


Fig. 5. Reaction mechanism on the catalyst, for the default conditions (see text). The gas-phase species are indicated in different colours, while the surface species are shown in black and marked with *. The colours of the arrows indicate which facet contributes to that reaction, as well as its relative contribution, represented by the ratio of colour length over total arrow length. Note that for most reactions the Ni(110) facet is dominant, and therefore most arrows are simply in blue. The arrow thickness shows the relative importance of that reaction in the overall mechanism, and the percentages corresponding to the different thicknesses are given in the legend. The percentages are calculated by dividing the rate of each reaction by the highest reaction rate in the mechanism: the associative recombination of $2H^*$ into H_2 . (For interpretation of the references to colour in this figure legend, the reader is referred to the web version of this article.)

with C* and CH* from CH₄ to create CO* and CHO* (which then dehydrogenates to CO*). This reaction primarily takes place on Ni(111) with minor activity observed on Ni(211) at the default parameter values, while in contrast, a reverse reaction on Ni(110) forms H_2O from O* and H*. The balance between both determines whether H_2O is produced or destroyed, but even though Ni(110) is the most active facet, H_2O is usually net consumed.

3.2.2. Parameter variations

Now that we have identified the reaction pathway at the default conditions, we will investigate how it changes at different conditions, and also study the effect of post-plasma catalysis on the $\rm CO_2$ and $\rm CH_4$ conversion and product distribution, attempting to determine the optimal value for the varied parameters.

(a) Site density

In Fig. 6, we show the effect of catalyst site density on the conversion of CO_2 and CH_4 and the contribution of the four different facets to CO formation. A plot with similar trends for facet contributions to H_2 production is given in Fig. S14 in the SI.

As shown in Fig. 6a, the $\rm CO_2$ and $\rm CH_4$ conversions without catalyst remain constant at 25 %, which is the default net gas fraction that can be converted by the plasma arc in the reactor. Upon catalyst addition, both the $\rm CO_2$ and $\rm CH_4$ conversion improve to the same extent at higher site densities, with a significant increase in conversion from $\rm 10^{18}~cm^{-3}$, demonstrating that post-plasma catalysis can indeed enhance $\rm CO_2$ and $\rm CH_4$ conversion in DRM. At site densities below $\rm 10^{18}~cm^{-3}$, no difference in conversion due to catalysis is observed, because the site density is too low for enough surface reactions to take place. Fig. 6a also indicates that maximising catalyst site density is key to achieving the highest possible conversions. However, in practice, the attainable site density is limited

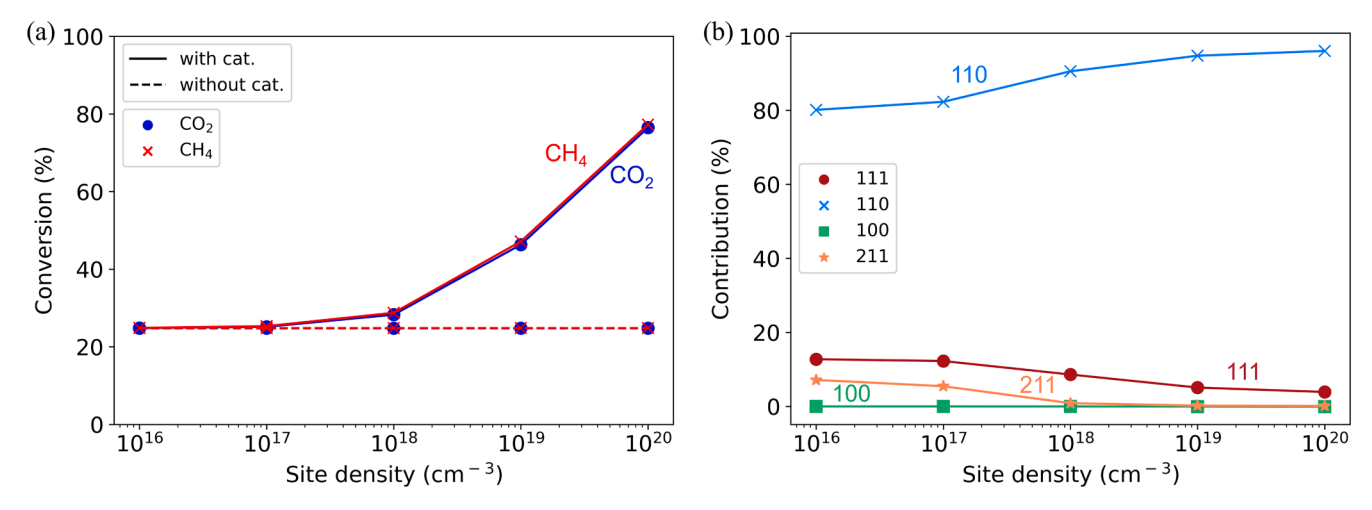


Fig. 6. Effect of catalyst site density on (a) conversion of CO_2 (blue) and CH_4 (red), both with (solid lines) and without (dashed lines) catalyst, and on (b) the contribution of every facet to the formation of CO. Note that the CO_2 and CH_4 curves in (a) overlap. (For interpretation of the references to colour in this figure legend, the reader is referred to the web version of this article.)

by synthesis, size and materials constraints. In our model, we used a default site density of $10^{19}~\rm cm^{-3}$, as detailed in the Method section, which is clearly sufficient for the catalyst to noticeably enhance conversion. As shown in Fig. 6a, while the overall trend remains consistent across different site densities, the magnitude of the catalytic effect varies – higher site densities yield a more pronounced increase in conversion.

The contributions of the four Ni facets as a function of site density (see Fig. 6b) are calculated by dividing the net desorption rate of CO or (in Section S2.2.3 in the SI) H₂ on a facet by the total net desorption rate over all facets, setting the value to 0 % when CO or H2 are adsorbed on that facet, meaning that the net desorption rate is negative (net desorption = desorption rate - adsorption rate). From this figure, it is clear that Ni(110) has by far the largest contribution, thus being the most active facet. This has already been reported before for CH₄ decomposition, where a Ni(110) single crystal was more active than Ni (100), which in turn had a higher activity than Ni(111) [117]. While the dominant contribution of Ni(110) is in good agreement with our model, our model predicts that Ni(111) is the second most active facet, albeit only slightly more active than the two remaining facets. The difference between Ni(100) and Ni(111) in our results and the results from Beebe Jr. et al. could be explained by the addition of CO2 and the lower pressure and temperature applied by Beebe Jr. et al. [117], as for our conditions Ni(100) is in most cases covered by C*. In addition, Ni(111) is the most abundant facet on the surface, accounting for 45 % of the total amount of surface sites, which can also explain its higher overall activity in our model compared to Ni(100), which accounts for only 10 % of the

The reason why Ni(110) is the most active facet is that Ni(110), as well as Ni(211), are step-edge facets, which have been demonstrated to have a higher activity for CH₄ dissociation than terrace facets like Ni (111) and Ni(100) [118]. Although Ni(110) has the highest contribution in our model for every site density investigated, at 10^{16} and 10^{17} cm⁻³ site densities Ni(111) and Ni(211) also have a non-negligible contribution, as can be seen in Fig. 6b. However, at these site densities, negligible CO₂ and CH₄ conversion is observed on the surface. Therefore, we should not dwell on the relative contribution of each facet at low site densities as their effect is very low. The same trends, but even more pronounced, i.e., with steeper gradients, are found for H₂ formation, which is shown in Fig. S14 in the SI.

(b) Gas temperature in the catalyst bed

The CO₂ and CH₄ conversions and surface coverages as a function of gas temperature in the catalyst bed are shown in Fig. 7, while Fig. S15 in

the SI presents the C* coverage results for the individual facets and the coverage results in more detail of less abundant, but nevertheless important, surface species.

The catalyst does not always improve the conversion of CO2 and CH4 when varying the temperature, unlike the site density scan. This leads to the general conclusion that adding a downstream catalyst is not always advantageous, and it depends on the conditions. For the temperature parameter specifically, below 900 K the calculated conversion of both CO₂ and CH₄ is lower upon catalyst addition. The shift to a beneficial scenario (i.e., the catalyst promotes extra conversion) depends on the chemical equilibrium composition: with increasing temperature, the products CO and H2 become more stable, thus the chemical equilibrium will shift towards these products, in the forward direction of the DRM reaction (Reaction (R.1) in the Introduction). However, at temperatures below 900 K and at 25 % conversion by the GAP reactor, CO2 and CH4 are more stable and some CO and H2 formed in the plasma react backwards at the catalyst into CO2 and CH4. In addition, the conversion can also be reduced by products adsorbing on the surface, lowering their concentration in the gas phase. This effect is especially pronounced at lower temperatures, where more species remain adsorbed on the surface (see Fig. 7b).

While we believe this trend will be generally valid, with a loss in conversion at lower temperatures and an increase at higher temperatures, it is possible that the shift in catalyst effect is located at another temperature, not exactly at 900 K. As shown for model validation, the chemical equilibrium composition in our thermodynamic input data is shifted to higher temperatures due to a change in the reaction enthalpy of DRM compared to its theoretical value. As a result, the transition temperature, i.e., when formation of CO and H₂ (and extra CO₂ and CH₄ conversion) begins to occur, may be located at lower temperatures than 900 K. Nevertheless, the general conclusions from this plot and model remain qualitatively valid.

As can be seen in Fig. 7a, the catalyst temperature should be as high as possible (up to 1200 K) to obtain the maximum increase in conversion with the catalyst, within experimental limits, such as carbon deposition and sintering. Therefore, it is important to control the gas temperature in the catalyst bed, which can be achieved by changing the position of the catalyst in the afterglow. The relationship between the temperatures and the distances between the catalyst and plasma zone is also plotted in Fig. 7a (with the corresponding temperatures from literature), which can help define the optimal position of the catalyst bed. In the studied range, we can conclude that the catalyst should be as close as possible to

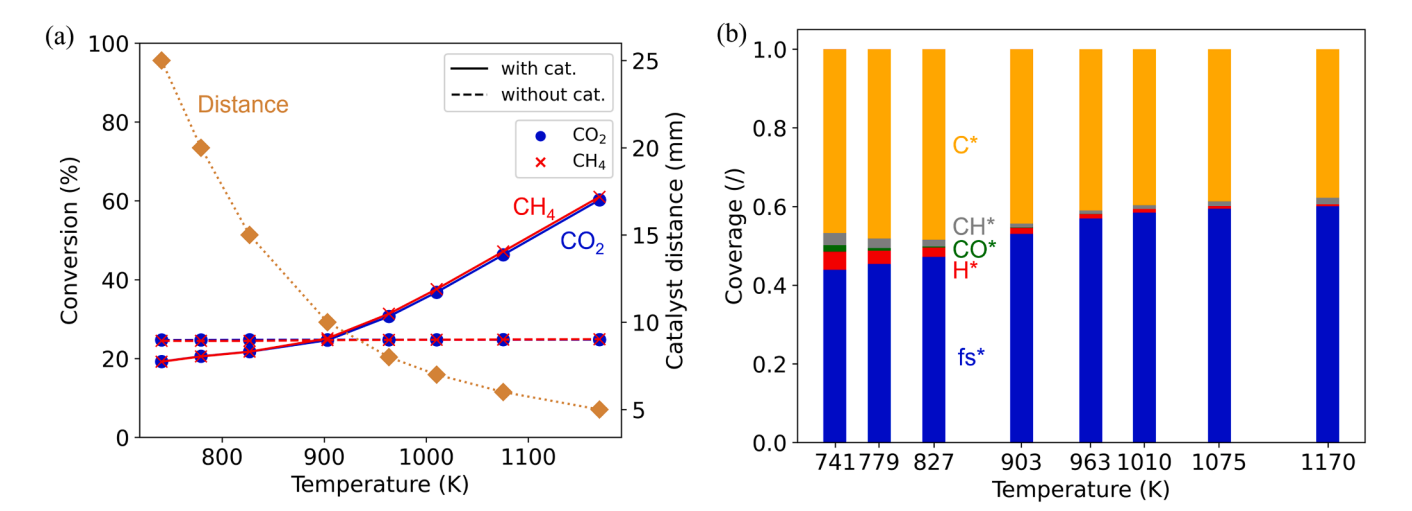


Fig. 7. (a) Conversion of CO₂ (blue) and CH₄ (red), both with (solid lines) and without (dashed lines) catalyst, as a function of gas temperature in the catalyst bed. Note that the CO₂ and CH₄ curves overlap. The distance of the catalyst bed post-plasma corresponding to each temperature is shown by a brown dotted line and given on a secondary y-axis. (b) Coverages of the main surface species and the fraction of free sites (fs*) on the surface for each simulated temperature. (For interpretation of the references to colour in this figure legend, the reader is referred to the web version of this article.)

the plasma. The effect of the catalyst position, showing the same graph types as presented here for the temperature variation, can be found in S2.2.1 of the SI.

The species coverage plot in Fig. 7b reveals that there is a large portion of free sites still available on the surface, ranging between approximately 40 and 60 %. Moreover, this fraction of free sites slightly increases with increasing temperatures. This can be explained by the fact that coverages of surface species decrease with increasing temperature [96].

Another conclusion that we can draw from Fig. 7b is that C* is clearly the most abundant species on the surface. Indeed, in Fig. S15a, the coverage of C* on each facet separately is included, illustrating that Ni (100) and Ni(211) are almost completely covered by C*, and these facets represent 10 % and 30 % of the surface, respectively, with only a slight decrease for Ni(211) with rising temperature. On the other hand, Ni (111) has an almost negligible C* coverage at all temperatures. Hence, the trend in C* coverage in Fig. 7b can be primarily ascribed to the change in C* coverage on Ni(110), which slightly increases between 741 K and 827 K, and then decreases to almost zero on Ni(110) above 1000 K (see Fig. S15a), causing a stagnation around 0.4 for the total C* coverage in Fig. 7b at these temperatures, between 1000 K and 1170 K, i. e., the highest simulated temperature. In literature, the same drop in carbon deposition with increasing temperature has been reported, also in the lower temperature range, where the C* formation is attributed to the Boudouard reaction [119-121]. However, as reaction rates in general increase with rising temperature, a trade-off, or balance between the increasing rate and the decreasing thermodynamic stability of C* leads to a maximum in the C* coverage around 800 K for our input conditions. This is also corroborated by Kennema and Rowntree, who observed a similar peak in carbon deposition around 600 °C, albeit Ar was present in their gas mixture [122]. Overall, the trends in C* coverage can be explained by the balance in thermodynamics and kinetics on Ni(110).

Apart from the most abundant species C* on the surface, the CH*, CO* and H* species also show appreciable coverage, as demonstrated in Fig. 7b. A more detailed graph with surface species with coverage below 0.1 is presented in Fig. S15b. In general, these coverages show the same, expected decreasing trend with increasing temperature.

The reaction mechanism for varying temperature remains unchanged with respect to the default parameter values, illustrated in Fig. 5, although the relative contributions of the different rates to the reaction network (arrow thickness) and the contributions of the facets

(colour distribution) can vary for different temperatures. However, at temperatures below 900 K, where reverse reactions take place, the same reaction mechanism is valid, but in the reverse direction, i.e., with all arrows pointing in the opposite direction, except for some reactions in the H₂O conversion branch. Along with the coverage plot in Fig. 7b, the reaction mechanism highlights an important effect of C* coverage. Clearly, C* participates in the main pathway, which is also demonstrated by its abundance on the surface. However, C* can also lead to C*poisoning, yielding a delicate balance, and temperatures above 1200 K can result in excessively high C* coverage and catalyst deactivation, as seen in the validation plots in Fig. 2 and Fig. 3.

(c) Plasma fraction

In this section, we vary the amount of gas that can be converted by the plasma before it arrives at the catalyst. Note again that this "plasma fraction" accounts not only for the fraction of gas passing through the plasma, but also for the fraction that is formed again by back-reactions of the products post-plasma, as explained in the Method section. Although this plasma fraction has no direct influence on the catalyst bed, it determines the gas mixture input in the catalyst CSTR. For this parameter, we discuss the ensuing variations in conversion in Fig. 8a, and molar product output fractions in Fig. 8b.

In the absence of a catalyst, we notice that the conversions of both CO2 and CH4 increase linearly with plasma fraction, which is logical, as more gas is being converted by the plasma. With catalyst, the conversion improves for all plasma fractions. Hence, irrespective of how much gas can be converted by the plasma, it is always advantageous to use a catalyst, in the range of conditions investigated here. This contrasts with the gas temperature, where a more delicate balance is present, as discussed above. The improvement in conversion upon catalyst addition is the largest for the lowest plasma fractions. This is also logical, because at lower plasma fractions, more CO2 and CH4 are left unconverted after the GAP reactor and can therefore be converted by the catalyst downstream. This is also reflected in the rates of the CO2 dissociation and CH4 dehydrogenation reactions, constituting the main reaction pathway, which increase with decreasing plasma fraction.

Although the effect of the catalyst is more pronounced at the lower plasma fractions, the highest overall conversions are still achieved at the largest plasma fractions. Hence, even at optimised plasma fractions, reaching the highest possible conversions by the plasma arc, the catalyst can still be useful to further boost the CO2 and CH4 conversions.

Similar trends are observed for the CO and H₂ molar output fractions in Fig. 8b. However, when comparing these to the chemical equilibrium

CO

0.4

 H_2O

0.3

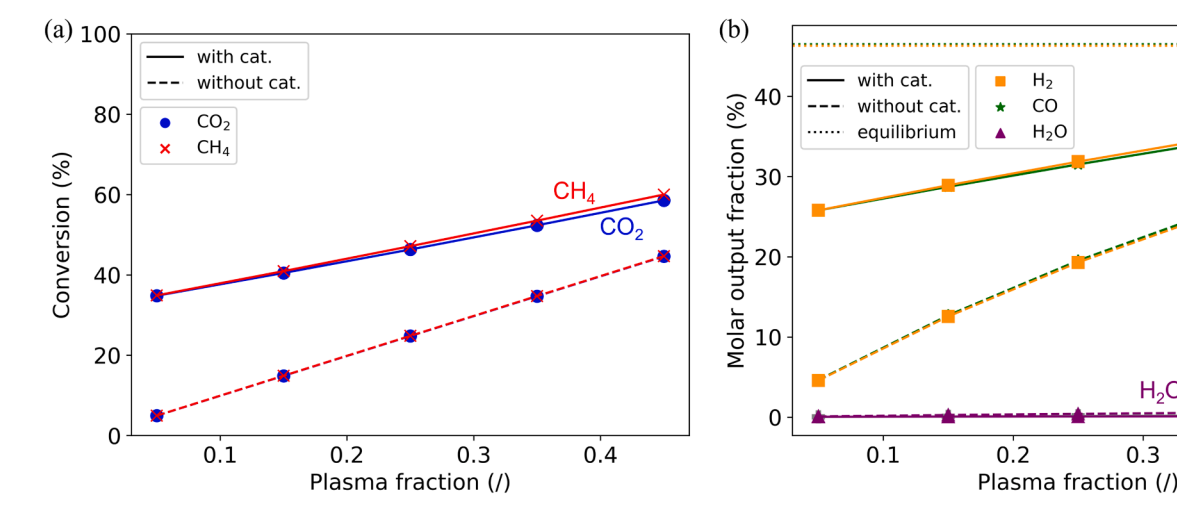


Fig. 8. Effect of plasma fraction (i.e., net fraction of gas that can be converted by the plasma) on (a) conversion of CO₂ (blue) and CH₄ (red), both with (solid lines) and without (dashed lines) catalyst, and on (b) the molar output fractions of the main products CO, H2 and H2O. Note that without catalyst, the CO2 and CH4 curves in (a) mostly overlap at every plasma fraction, while in (b) the output fractions of CO and H₂ without catalyst overlap, and the H₂O output fractions with and without catalyst also overlap. In (b) the chemical equilibrium molar fraction of CO and H2 is indicated with a dotted line, at 1075 K, which corresponds to the gas temperature in the catalyst bed for these simulations. (For interpretation of the references to colour in this figure legend, the reader is referred to the web version of this article.)

composition curves (dotted lines in Fig. 8b), one important conclusion is that chemical equilibrium is not reached at the end of the catalyst bed at the conditions under study. Indeed, both the CO and H2 molar fractions are lower than their chemical equilibrium fractions, around 46-47 % at 1075 K, i.e., the gas temperature in the catalyst bed. As discussed in the previous section, the balance between improving or reducing the conversion upon catalyst addition depends on which species are more stable, the reactants CO₂ and CH₄ or the products CO and H₂, which is determined by the chemical equilibrium composition. Because this chemical equilibrium composition in turn varies with temperature, there is a correlation between the conversion and direction of the DRM reaction (R.1) on one hand, and the gas temperature in the catalyst bed (or bed position) on the other hand. However, this correlation only holds perfectly if the chemical equilibrium composition is indeed reached by the gas mixture at the end of the catalyst bed. Since this is not the case, not only thermodynamics, but also kinetics play a role and influence the final conversions, and we cannot entirely predict the effect of the temperature (and thus catalyst bed position) based on the chemical equilibrium composition alone. Indeed, in this case, the effect of the catalyst on the results also depends on the input conditions, such as the flow rate, which determines the residence time. Nonetheless, as evidenced by this analysis, the positive effect of the catalyst can still be optimised, aiming to reach the chemical equilibrium compositions by changing these input conditions. Overall, this illustrates that a detailed model, as presented in this work, is required to gain such insight, because it cannot be simply deduced from chemical equilibrium compositions.

Upon analysis of both plots in Fig. 8, we note that at plasma fractions above 25 %, slightly more CH₄ is converted by the catalyst than CO₂, which is also reflected in the H₂ molar output fraction being slightly higher than that of CO. This can be explained by a higher C* coverage on Ni(110), which means that CH₄ is being converted and dehydrogenated, creating H₂. However, as C* accumulates on the surface, CO cannot be concomitantly formed, in turn leading to slightly less CO₂ dissociation and formation of CO. As a result, the syngas ratio will also be slightly higher than 1, increasing with rising plasma fraction. The H₂O curve in Fig. 8b and the effect of the plasma fraction on the reaction mechanism are discussed in Section S2.2.5 in the SI.

(d) Input gas mixture

Fig. 9 illustrates the CO_2 and CH_4 conversion (a), and the molar output fractions of the most important products (b), as a function of CO_2 fraction in the input gas. To explain the trends and investigate the more practical aspects of this parameter variation, we also plot the rates of the most important reactions involving O^* , as well as the syngas ratio, in

Fig. 10 a and b, respectively. In this case, the C-, H- and O-based selectivities also exhibit variations, due to the formation of C_2H_2 and H_2O at some of the input gas mixtures, and this is shown and discussed in Fig. S19 and Section S2.2.6 in the SI.

In Fig. 9a, we can see that without catalyst, CH_4 is fully converted for all input gas mixtures, corresponding to a conversion of 25 % as determined by the plasma fraction (also set to 25 %). However, this is not the case for CO_2 , which exhibits a drop in conversion at CO_2 input fractions above 50 %. This was also observed in the simulations by Slaets et al. [42]. Below 50 % CO_2 input fractions, the excess CH_4 (relative to stoichiometric DRM) can be converted into H_2 and C_2H_2 , not requiring CO_2 molecules, whereas the CO_2 conversion is clearly enhanced by the presence of CH_4 , except at higher CO_2 input fractions (and thus lower CH_4 input fractions), leading to a lower CO_2 conversion there. Indeed, the CO_2 conversion is typically enhanced upon CH_4 addition [3,42]. The production of C_2H_2 at low CO_2 fractions seen in Fig. 9b corroborates this rationale

Upon catalyst addition, we see an improvement in both $\rm CO_2$ and $\rm CH_4$ conversions, rendering post-plasma catalysis beneficial for all input gas mixtures investigated (except at the lowest $\rm CO_2$ input fraction; see below). With increasing $\rm CO_2$ input fraction, a clear rising trend is observed for the $\rm CH_4$ conversion, while the $\rm CO_2$ conversion drops again at $\rm CO_2$ input fractions above 30 %. This can be explained by the fact that the conversions plotted here are absolute conversions, and the $\rm CO_2$ conversion typically improves upon $\rm CH_4$ addition. The lack of conversion enhancement for both $\rm CO_2$ and $\rm CH_4$ upon catalyst addition at the lowest $\rm CO_2$ input fraction can be again explained by $\rm C^*$ -poisoning. This can also be seen in the coverage plot in Fig. S18a in the SI. This $\rm C^*$ coverage is particularly pronounced on Ni(110) in the 10–30 % $\rm CO_2$ input range. As this is the most active facet (see Section 3.2.2(a)), this limits the enhancement in overall $\rm CO_2$ and $\rm CH_4$ conversion.

For the $\rm H_2$ molar output fraction in Fig. 9b, an overall drop is observed (without catalyst, and above 30 % with catalyst) with increasing $\rm CO_2$ input fractions, and therefore decreasing $\rm CH_4$ input fractions, because $\rm H_2$ is mainly formed from $\rm CH_4$ dehydrogenation. The maximum at 30 % with catalyst can be explained by the higher $\rm C^*$ coverage at lower $\rm CO_2$ input fractions, as mentioned above. On the other hand, the CO molar fraction reaches a maximum at a 50/50 $\rm CO_2/\rm CH_4$ ratio, because its formation is related to both $\rm CO_2$ dissociation and $\rm C^*$ (formed from $\rm CH_4$) oxidation, as explained in Fig. 5 above. A more detailed explanation is given in Section S2.2.6 in the SI.

In addition, our model shows that H_2O is formed in the plasma at CO_2 input fractions above 50 % due to the reverse water gas shift reaction,

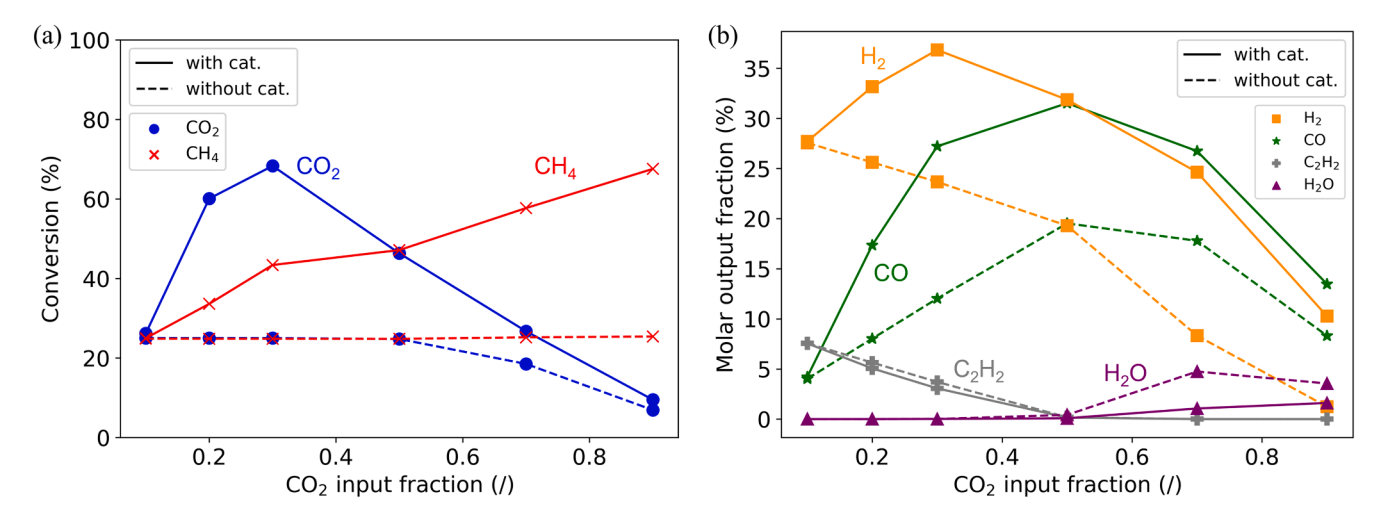


Fig. 9. Effect of the CO_2 fraction in the input gas on (a) conversion of CO_2 (blue) and CH_4 (red), both with (solid lines) and without (dashed lines) catalyst, and on (b) the molar output fractions of the main products CO, H_2 , H_2O and C_2H_2 . Note that the curves for CO_2 and CH_4 without catalyst in (a) overlap below 50 % CO_2 , while in (b) the H_2O molar fraction below 50 % CO_2 and the C_2H_2 molar fraction above 50 % CO_2 with and without catalyst overlap. (For interpretation of the references to colour in this figure legend, the reader is referred to the web version of this article.)

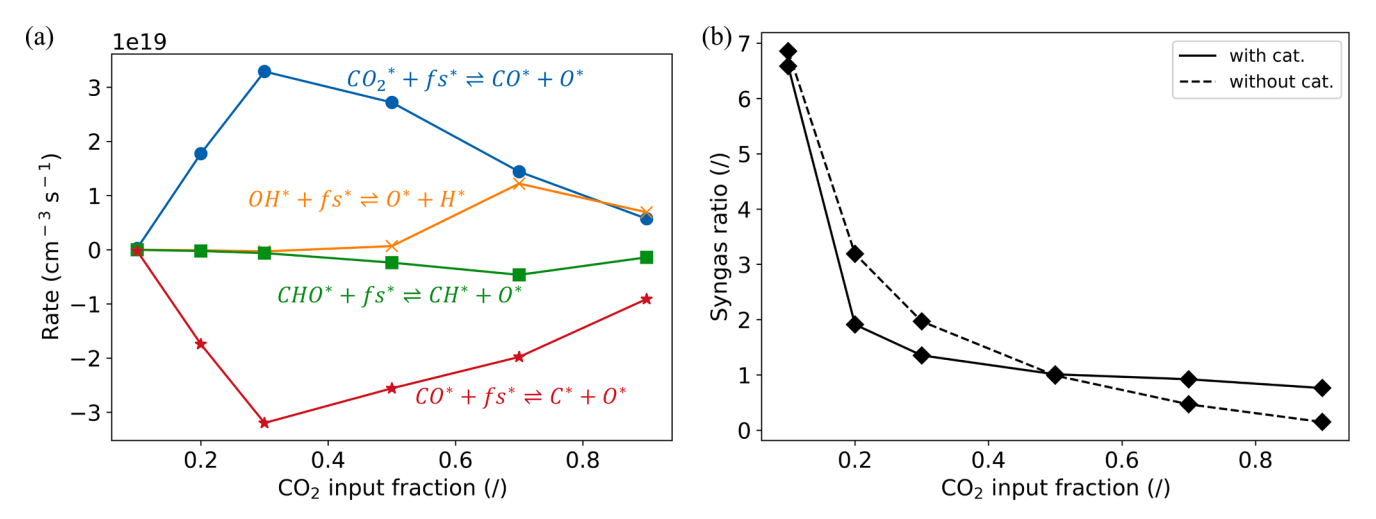


Fig. 10. Effect of the CO_2 fraction in the input gas on (a) rates of the most important reactions involving O^* , because O^* connects the conversion of CO_2 , CH_4 and H_2O in the reaction mechanism, and (b) the syngas ratio with (solid line) and without (dashed line) catalyst. Negative rates in (a) signify that the backward reaction is happening, consuming O^* .

which converts CO_2 and H_2 (originated from DRM) into CO and H_2O . This is in line with the model developed by Slaets et al. [42]. As can be seen in Fig. 9b, this H_2O can react with CH_4 and be converted into H_2 and CO in the presence of catalyst, resulting in lower H_2O output fractions upon catalyst addition. This conversion can be confirmed by the surface coverages in Fig. S18 in the SI, where a clear rise in the O^* and OH^* coverages above 50 % CO_2 is observed on the Ni facets, especially on Ni(211). Since H_2O is an unwanted by-product from DRM, this indication of H_2O conversion by the catalyst is an extra advantage, in addition to improving the conversion of CO_2 and CH_4 . However, we must be cautious with this result, since the validation in Section 3.1 has shown that H_2O conversion can be overestimated by the model, as the chemical equilibrium composition of H_2O using the shifted reaction enthalpies shows no H_2O formation at any temperature.

From a mechanistic perspective, Fig. 10a displays a plot with the rates of the most important reactions involving O*. Indeed, as can be seen in the reaction mechanism in Fig. 5, O* connects the conversion pathways of the two reactants CO2 and CH4 (it is formed upon CO2* dissociation into CO* and O*, and reacts with C* from CH4 to form another CO*), and is also created through the conversion of H2O, making it an important intersection in the reaction mechanism network. In this way, it allows us to draw three main conclusions, i.e., about H₂O conversion, as well as the rate-limiting steps in ${\rm CO_2}$ and ${\rm CH_4}$ conversion. These are discussed below, while a more elaborate analysis of the plot is given in Section S2.2.6 in the SI. Firstly, the rate of OH* dissociation into O* and H* (orange curve) is higher above 50 % CO2 input, which is caused by H₂O conversion (producing OH*), also observed in Fig. 9b and discussed above. Secondly, the CO₂* dissociation rate (blue curve) reaches a maximum at 30 % CO2 input fraction, which indicates that the CH₄ dehydrogenation steps are rate-limiting, causing the rates of CH₄ and CO2 conversion to rise with decreasing CO2 input fractions (and therefore increasing CH₄ input fractions). However, the higher CH* and especially C* coverages, in particular at large CH4 input fractions, shown in Fig. S18, suggest that carbon oxidation ($C^* + O^*$ into CO^* , red curve, with negative rates, indicating that the reaction proceeds in the opposite direction) may also be a rate-limiting step. For a quantitative assessment, a sensitivity analysis was carried out, similar to the degree of rate control analysis presented by Campbell [123]. The employed methodology of this degree of rate control sensitivity analysis is described in Section S2.2.6 of the SI. The results show that the overall rate-limiting step, both at default input conditions (50 % CO2), as well as at the conditions corresponding to the highest rates for O* production and consumption (30 % CO₂), is one of the CH₄ dehydrogenation steps, namely the dissociative adsorption of CH₄ (Reaction (R.2)). The other

dehydrogenation steps, on the other hand, exhibit much lower ratelimiting potential and their contribution to the overall DRM rate can be neglected under the conditions tested in our model. Two other reactions in the mechanism that influence the overall rate are the carbon oxidation step (Reaction (R.3)), as mentioned above, albeit this sensitivity analysis ascertains that the dissociation of CO₂* (Reaction (R.4)) has a slightly larger effect on the DRM rate. Indeed, upon changing the rate coefficients, the CO₂* dissociation rate has a stronger effect (up to 3 times) on the overall DRM rate, compared to carbon oxidation. This explains why, although an increase in C* coverage is observed when carbon oxidation is rate-limiting, a concomitant increase does not occur for the O* coverage, as the latter is produced by the more rate-limiting CO₂* dissociation reaction. All of these processes have been confirmed to be possible rate-limiting steps by literature [114–116,124]. The plots for this degree of rate control analysis are presented in Figs. S16 and S17. Finally, building upon our second conclusion, a balance in C* can be determined. Indeed, the rates of the blue and red curve increase with decreasing CO2 and increasing CH4 input fractions, which is beneficial for the results, producing more CO*, but when too much CH₄ is added, starting below 30 % CO2 and above 70 % CH4, C*-poisoning can take place, decreasing the CO* formation rates again.

$$CH_4 + fs^* + fs^* \rightleftharpoons CH_3^* + H^*$$
 (R.2)

$$C^* + O^* \rightleftharpoons CO^* + fs^* \tag{R.3}$$

$$CO_2^* + fs^* = CO^* + O^*$$
 (R.4)

Fig. 10b presents the syngas (i.e., H_2/CO) ratio (see Eq. (17)), which is important for later applications of the product gas mixture, where usually a syngas ratio of 2 is preferred, e.g., in methanol or Fischer-Tropsch synthesis. The syngas ratio drops with increasing CO_2 input fractions with and without catalyst, which is logical, due to lower CH_4 fractions, ensuing less H_2 formation. When a catalyst is added, the syngas ratio is reduced below 50 % CO_2 input, because in this range the CO_2 conversion is higher, as explained above and as shown in Fig. 10a for the higher CO^* production rate from CO_2^* . Above 50 % CO_2 input, however, the catalyst increases the syngas ratio, because extra H_2 is produced from the conversion of H_2O , while not all O^* can react into CO due to the limited C^* supply stemming from the lower CH_4 input (see red curve in Fig. 10a).

Finally, besides scanning the gas temperature in the catalyst bed at a default input gas mixture (see previous section (b)) and the input gas mixture with a default temperature profile (this section), we also varied

both simultaneously and the results are explained in Section S2.2.6. Most notably, when varying the temperature using a gas mixture of 30 % $\rm CO_2$ and 70 % $\rm CH_4$, we see a positive effect on $\rm CO_2$ conversion below 900 K compared to the 50/50 input ratio and a syngas ratio above 1 at all temperatures, albeit at the cost of an increased tendency for C*-poisoning.

In conclusion, combining the analysis of the syngas ratio with the conversions and molar outputs, we can postulate the $30/70~\mathrm{CO}_2/\mathrm{CH}_4$ ratio as the optimal gas input for the utilisation of post-plasma catalysis in DRM. At this ratio, the syngas ratio is above 1 (although not equal to 2) and in addition, no C*-poisoning is observed, unlike at higher CH₄ fractions. Furthermore, the reaction rates of CO₂ and CH₄ conversion and CO and H₂ formation reach a maximum at this input gas mixture. Finally, the CO₂ and CH₄ conversions are both relatively high, and the total (CO₂ + CH₄) conversion reaches a maximum of 51 % at the $30/70~\mathrm{CO}_2/\mathrm{CH}_4$ ratio.

To have a general overview, we evaluate the influence of the most important parameters, i.e., temperature and input gas mixture, on the syngas ratio, reaction selectivity and energy efficiency, while avoiding C*-poisoning. The input gas mixture primarily affects the syngas ratio and selectivity: higher CH₄ fractions increase the syngas ratio but also increase the risk of C*-poisoning, while higher CO2 fractions reduce C*poisoning but lower the syngas ratio and selectivity of favourable products, leading to unwanted H2O formation that can still be converted by the catalyst. Temperature mainly impacts energy efficiency, since higher temperatures enhance reaction rates, conversion, and energy efficiency, but only if the gain in conversion compensates for the higher power demand. Beyond a threshold temperature, however, C*poisoning occurs (see Fig. 2 and Fig. 3 in Section 3.1), reducing both conversion and energy efficiency, highlighting the need for a balance in gas temperature. Finally, it should be noted that C* coverage is not always detrimental. Moderate C* coverage can increase the syngas ratio (see Fig. 10b), although excessive C* coverage reduces catalyst reactivity. Overall, several factors determine the catalyst's performance and the trends as a function of these parameters highlighted in this paper can serve as a guide for further optimisation of experimental implementation of post-plasma Ni catalysis for DRM.

4. Conclusion

We developed a 0D microkinetic model, describing the chemistry in the plasma, its afterglow and at the catalyst surface, to investigate the effect of a Ni catalyst on the $\rm CO_2$ and $\rm CH_4$ conversion, production of $\rm H_2$ and $\rm CO$ and syngas ratio downstream from a warm plasma for DRM.

We first validated our model against two separate sets of experiments from literature, focussing mostly on verifying the surface reaction network and DFT input data used to calculate the surface reaction rates. From the validation study, we can draw three main conclusions. (i) The overall chemical equilibrium composition is shifted to ~100 K higher temperatures than the theoretical values, caused by a deviation in the overall DRM reaction enthalpy calculated from the DFT data used in the model. This results in lower conversions at specific temperatures than theoretically expected, though this will not influence the trends or overall conclusions. (ii) At some conditions, especially at higher temperatures, C*-poisoning can take place on the surface and prevent the effect of the catalyst. Finally, (iii) a sensitivity analysis reveals that the formation of H₂O is underestimated in the model, which can also be attributed to the DFT input data. In general, however, the validation shows that the model is able to capture well the trends observed in the experiments.

As a consequence, we applied our model to study the effect of post-plasma catalysis with a GAP reactor, to answer two questions: (i) Can the conversion be improved by post-plasma catalysis? and (ii) What is the reaction mechanism behind the observed trends? We demonstrated that the conversion can indeed be improved by post-plasma catalysis. However, this improvement depends on specific reaction conditions, and

some conditions, such as temperatures below 900 K, lead to a drop in ${\rm CO}_2$ and ${\rm CH}_4$ conversion upon adding a catalyst. We also identified the optimal values for a wide range of studied parameters. More specifically, the catalyst surface site density, gas temperature in the catalyst bed and plasma fraction (i.e., fraction of gas that can be converted by the plasma) should be as high as possible, within experimental limits and considering possible C*-poisoning at higher temperatures. As for the input gas mixture, the best results are reached for a 30/70 ${\rm CO}_2/{\rm CH}_4$ ratio, improving the ${\rm CO}_2$ and ${\rm CH}_4$ conversion from 25 % to 68 % and from 25% to 43 %, respectively, upon catalyst addition, with flexibility for the syngas ratio depending on the application of the final gas mixture.

The model does not only analyse the catalyst's effects on conversion and product output, but also the most important reaction pathways. For most conditions, CH4 dissociatively adsorbs on the surface and sequentially dehydrogenates up to C*, which can then combine with O* from CO₂* dissociation to form CO*, while the H* species recombine to form H₂. Other pathways can also occur for specific reaction conditions, such as the formation of CHO*, of which the subsequent dehydrogenation contributes to 4.3 % of the CO* formation at default conditions. In addition, H₂O (when formed in the plasma) can be converted by the catalyst surface, e.g. at CO₂ input fractions above 50 %, reducing the concentration of this unwanted by-product in the gas phase, though the quantitative accuracy of the conversion predicted by the model is limited by the DFT input data. Overall, however, the mechanism of syngas formation remains mostly unchanged in the wide range of conditions investigated. From this mechanism analysis, we conclude that C* is an essential species to the reaction pathways, having the highest coverage on the surface; but C* accumulation can also cause catalyst poisoning and deactivation, leading to a delicate balance. Finally, the model also allows us to investigate the contribution of each facet to this reaction mechanism, with Ni(110) being the most active facet overall, although the H₂O conversion to O* and 2H*, discussed above, takes place mostly on Ni(111) and Ni(211).

Although the constructed model was successful for our two research questions, there is scope for further improvements. The model is now only able to calculate the effect on the conversion, but cannot predict the energy efficiency, which is also important for practical applications. To assess this aspect, an energy balance must be included in the model, which would allow the model to calculate the temperature selfconsistently instead of using a temperature profile from literature. In addition, transport phenomena should be incorporated, including transport of species in the gas phase and diffusion to and interaction with the surface, as mass transport to and from the catalyst can be very important, and our model assumes no transport limitations. These improvements require a higher dimensional model, which will be the focus of our future work. Nonetheless, the present model is useful to guide experimental work towards improved output by tuning certain parameters, e.g., increasing the gas temperature inside the catalyst bed, or tweaking the catalyst synthesis to increase the site density, or shift the facet distribution to a higher Ni(110) contribution. Overall, we have shown the promising positive effect of post-plasma catalysis on the conversion and product output from the DRM reaction.

CRediT authorship contribution statement

Sara Ceulemans: Writing – original draft, Visualization, Validation, Software, Methodology, Investigation, Formal analysis, Conceptualization. Eduardo Morais: Writing – review & editing, Supervision, Methodology. Björn Loenders: Software, Methodology, Conceptualization. Annemie Bogaerts: Writing – review & editing, Supervision, Project administration, Funding acquisition.

Declaration of competing interest

The authors declare the following financial interests/personal relationships which may be considered as potential competing interests:

Sara Ceulemans reports financial support was provided by Research Foundation Flanders. If there are other authors, they declare that they have no known competing financial interests or personal relationships that could have appeared to influence the work reported in this paper.

Acknowledgements

This work was supported by the Research Foundation - Flanders (FWO, grant No 1101524N), as well as the European Research Council (ERC) under the European Union's Horizon 2020 research and innovation programme (grant agreement No 810182 – SCOPE ERC Synergy project).

Appendix A. Supplementary data

Supplementary data to this article can be found online at https://doi.org/10.1016/j.jcat.2025.116474.

Data availability

Data will be made available on request.

References

- United Nations Framework Convention on Climate Change (UNFCCC), Paris Agreement, (2015).
- [2] IPCC, Climate Change 2023: Synthesis Report, 2023.
- [3] R. Snoeckx, A. Bogaerts, Plasma technology a novel solution for CO2 conversion? Chem. Soc. Rev. 46 (2017) 5805–5863, https://doi.org/10.1039/ C6CS00066F
- [4] T. Lieuwen, V. Yang, R. Yetter, Synthesis Gas Combustion: Fundamentals and Applications, CRC Press, 2009 https://books.google.be/books? id=qNTPbVCzx9MC.
- [5] C. Song, CO2 conversion and utilization: an overview, in: C. Song, A.F. Gaffney, K. Fujimoto (Eds.), CO2 Convers. Util., American Chemical Society, Washington, 2002, pp. 2–30, https://doi.org/10.1021/bk-2002-0809.
- [6] B. Wanten, S. Maerivoet, C. Vantomme, J. Slaets, G. Trenchev, A. Bogaerts, Dry reforming of methane in an atmospheric pressure glow discharge: confining the plasma to expand the performance, J. CO2 Util. 56 (2022) 101869, https://doi.org/10.1016/j.jcou.2021.101869.
- [7] Y. Zeng, X. Zhu, D. Mei, B. Ashford, X. Tu, Plasma-catalytic dry reforming of methane over γ-Al2O3 supported metal catalysts, Catal. Today 256 (2015) 80–87, https://doi.org/10.1016/j.cattod.2015.02.007.
- [8] R. Snoeckx, Y.X. Zeng, X. Tu, A. Bogaerts, Plasma-based dry reforming: improving the conversion and energy efficiency in a dielectric barrier discharge, RSC Adv. 5 (2015) 29799–29808, https://doi.org/10.1039/C5RA01100K.
- [9] Z. Farshidrokh, M.R. Khani, A. Khodadadi, M. Gharibi, B. Shokri, Dry reforming of methane over Ni/γ-MgO catalysts in a coaxial dielectric barrier discharge reactor, Chem. Eng. Technol. 44 (2021) 589–599, https://doi.org/10.1002/ ceat.202000455.
- [10] D. Mei, B. Ashford, Y.-L. He, X. Tu, Plasma-catalytic reforming of biogas over supported Ni catalysts in a dielectric barrier discharge reactor: effect of catalyst supports, Plasma Process. Polym. 14 (2017) 1600076, https://doi.org/10.1002/ ppap.201600076.
- [11] J. Wang, K. Zhang, V. Meynen, A. Bogaerts, Dry reforming in a dielectric barrier discharge reactor with non-uniform discharge gap: effects of metal rings on the discharge behavior and performance, Chem. Eng. J. 465 (2023) 142953, https:// doi.org/10.1016/j.cej.2023.142953.
- [12] D. Mei, G. Duan, J. Fu, S. Liu, R. Zhou, R. Zhou, Z. Fang, P.J. Cullen, K. (Ken) Ostrikov, CO2 reforming of CH4 in single and double dielectric barrier discharge reactors: comparison of discharge characteristics and product distribution, J. CO2 Util. 53 (2021) 101703, https://doi.org/10.1016/j.jcou.2021.101703.
- [13] X. Zhang, M.S. Cha, Electron-induced dry reforming of methane in a temperature-controlled dielectric barrier discharge reactor, J. Phys. D Appl. Phys. 46 (2013) 415205, https://doi.org/10.1088/0022-3727/46/41/415205.
- [14] J. Kim, M.S. Abbott, D.B. Go, J.C. Hicks, Enhancing C-H bond activation of methane via temperature-controlled, catalyst-plasma interactions, ACS Energy Lett. 1 (2016) 94-99, https://doi.org/10.1021/acsenergylett.6b00051.
- [15] X. Tu, J.C. Whitehead, Plasma dry reforming of methane in an atmospheric pressure AC gliding arc discharge: co-generation of syngas and carbon nanomaterials, Int. J. Hydrogen Energy 39 (2014) 9658–9669, https://doi.org/ 10.1016/j.jihydene.2014.04.073.
- [16] Y. Xia, N. Lu, B. Wang, J. Li, K. Shang, N. Jiang, Y. Wu, Dry reforming of CO2-CH4 assisted by high-frequency AC gliding arc discharge: electrical characteristics and the effects of different parameters, Int. J. Hydrogen Energy 42 (2017) 22776–22785, https://doi.org/10.1016/j.ijhydene.2017.07.104.
- [17] E. Cleiren, S. Heijkers, M. Ramakers, A. Bogaerts, Dry reforming of methane in a gliding arc plasmatron: towards a better understanding of the plasma chemistry, ChemSusChem 10 (2017) 4025–4036, https://doi.org/10.1002/cssc.201701274.

- [18] J. Martin-del-Campo, S. Coulombe, J. Kopyscinski, Influence of operating parameters on plasma-assisted dry reforming of methane in a rotating gliding arc reactor, Plasma Chem. Plasma Process. 40 (2020) 857–881, https://doi.org/ 10.1007/s11090-020-10074-2.
- [19] D.K. Dinh, G. Trenchev, D.H. Lee, A. Bogaerts, Arc plasma reactor modification for enhancing performance of dry reforming of methane, J. CO2 Util. 42 (2020) 101352, https://doi.org/10.1016/j.jcou.2020.101352.
- [20] J.-L. Liu, Y. Gao, B. Sun, B. Zhu, X.-S. Li, A.-M. Zhu, Mechanism study on gliding arc (GA) plasma reforming: a combination approach of experiment and modeling, Plasma Process. Polym. 19 (2022) 2200077, https://doi.org/10.1002/ ppap.202200077.
- [21] E. Devid, D. Zhang, D. Wang, M. Ronda-Lloret, Q. Huang, G. Rothenberg, N. R. Shiju, A.W. Kleyn, Dry Reforming of methane under mild conditions using radio frequency plasma, Energy Technol. 8 (2020) 1900886, https://doi.org/10.1002/ente.201900886.
- [22] P. Capezzuto, F. Cramarossa, R. D'Agostino, E. Molinari, Cracking and oxidation of methane under electrical discharge in the presence of carbon dioxide, water vapor and oxygen, Combust. Flame 33 (1978) 251–262, https://doi.org/ 10.1016/0010-2180(78)90064-0.
- [23] S. Kelly, E. Mercer, R. De Meyer, R.-G. Ciocarlan, S. Bals, A. Bogaerts, Microwave plasma-based dry reforming of methane: reaction performance and carbon formation, J. CO2 Util. 75 (2023) 102564, https://doi.org/10.1016/j. icou.2023.102564.
- [24] S.M. Chun, Y.C. Hong, D.H. Choi, Reforming of methane to syngas in a microwave plasma torch at atmospheric pressure, J. CO2 Util. 19 (2017) 221–229, https:// doi.org/10.1016/j.jcou.2017.03.016.
- [25] S.M. Chun, D.H. Shin, S.H. Ma, G.W. Yang, Y.C. Hong, CO2 microwave plasma—catalytic reactor for efficient reforming of methane to syngas, Catalysts 9 (2019) 292, https://doi.org/10.3390/catal9030292.
- [26] X. Zhang, N. Kobayashi, A. Suami, Y. Itaya, Reforming of methane and carbon dioxide to C2 hydrocarbons in microwave plasma at atmosphere pressure, J. Chem. Eng. Japan 57 (2024) 2387919, https://doi.org/10.1080/ 00219592.2024.2387919.
- [27] H. Sun, J. Lee, M.S. Bak, Experiments and modeling of atmospheric pressure microwave plasma reforming of a methane-carbon dioxide mixture, J. CO2 Util. 46 (2021) 101464, https://doi.org/10.1016/j.jcou.2021.101464.
- [28] O. Biondo, C.F.A.M. van Deursen, A. Hughes, A. van de Steeg, W. Bongers, M.C. M. van de Sanden, G. van Rooij, A. Bogaerts, Avoiding solid carbon deposition in plasma-based dry reforming of methane, Green Chem. 25 (2023) 10485–10497, https://doi.org/10.1039/D3GC03595F.
- [29] L. Zhang, S. Heijkers, W. Wang, L.M. Martini, P. Tosi, D. Yang, Z. Fang, A. Bogaerts, Dry reforming of methane in a nanosecond repetitively pulsed discharge: chemical kinetics modeling, Plasma Sources Sci. Technol. 31 (2022) 055014, https://doi.org/10.1088/1361-6595/ac6bbc.
- [30] C. Montesano, M. Faedda, L.M. Martini, G. Dilecce, P. Tosi, CH4 reforming with CO2 in a nanosecond pulsed discharge. The importance of the pulse sequence, J. CO2 Util. 49 (2021) 101556, https://doi.org/10.1016/j.jcou.2021.101556.
- [31] P.D.G. Maqueo, S. Coulombe, J.M. Bergthorson, Energy efficiency of a nanosecond repetitively pulsed discharge for methane reforming, J. Phys. D Appl. Phys. 52 (2019) 274002, https://doi.org/10.1088/1361-6463/ab199b.
- [32] M. Scapinello, L.M. Martini, G. Dilecce, P. Tosi, Conversion of CH4 /CO2 by a nanosecond repetitively pulsed discharge, J. Phys. D Appl. Phys. 49 (2016) 075602, https://doi.org/10.1088/0022-3727/49/7/075602.
- [33] D.L. Kuznetsov, V.V. Uvarin, I.E. Filatov, Conversion of methane in plasma of pulsed nanosecond discharges, IEEE Trans. Plasma Sci. 49 (2021) 2604–2612, https://doi.org/10.1109/TPS.2021.3075101.
- [34] M.-W. Li, Y.-L. Tian, G.-H. Xu, Characteristics of carbon dioxide reforming of methane via alternating current (AC) corona plasma reactions, Energy Fuel 21 (2007) 2335–2339, https://doi.org/10.1021/ef070146k.
- [35] H.H. Nguyen, A. Nasonova, I.W. Nah, K.-S. Kim, Analysis on CO2 reforming of CH4 by corona discharge process for various process variables, J. Ind. Eng. Chem. 32 (2015) 58–62, https://doi.org/10.1016/j.jiec.2015.07.018.
- [36] M.-W. Li, C.-P. Liu, Y.-L. Tian, G.-H. Xu, F.-C. Zhang, Y.-Q. Wang, Effects of catalysts in carbon dioxide reforming of methane via corona plasma reactions, Energy Fuel 20 (2006) 1033–1038, https://doi.org/10.1021/ef050207j.
- [37] D. Li, X. Li, M. Bai, X. Tao, S. Shang, X. Dai, Y. Yin, CO2 reforming of CH4 by atmospheric pressure glow discharge plasma: a high conversion ability, Int. J. Hydrogen Energy 34 (2009) 308–313, https://doi.org/10.1016/j. ijhydene.2008.10.053.
- [38] A. Fridman, Plasma Chemistry, Cambridge University Press, Cambridge, 2008, 10.1017/CBO9780511546075.
- [39] T.P. Nunnally, Application of Low Current Gliding Arc Plasma Discharges for Hydrogen Sulfide Decomposition and Carbon Dioxide Emission Reduction, Drexel University, 2011, 10.17918/00007845.
- [40] G. Trenchev, S. Kolev, W. Wang, M. Ramakers, A. Bogaerts, CO2 conversion in a gliding arc plasmatron: multidimensional modeling for improved efficiency, J. Phys. Chem. C 121 (2017) 24470–24479, https://doi.org/10.1021/acs. ipcc 7b08511
- [41] J.-L. Liu, X. Wang, X.-S. Li, B. Likozar, A.-M. Zhu, CO2 conversion, utilisation and valorisation in gliding arc plasma reactors, J. Phys. D Appl. Phys. 53 (2020) 253001, https://doi.org/10.1088/1361-6463/ab7c04.
- [42] J. Slaets, B. Loenders, A. Bogaerts, Plasma-based dry reforming of CH4: plasma effects vs. thermal conversion, Fuel 360 (2024) 130650, https://doi.org/ 10.1016/j.fuel.2023.130650.

- [43] M. Ramakers, G. Trenchev, S. Heijkers, W. Wang, A. Bogaerts, Gliding arc plasmatron: providing an alternative method for carbon dioxide conversion, ChemSusChem 10 (2017) 2642–2652, https://doi.org/10.1002/cssc.201700589.
- [44] G. Trenchev, A. Bogaerts, Dual-vortex plasmatron: a novel plasma source for CO2 conversion, J. CO2 Util. 39 (2020) 101152, https://doi.org/10.1016/j.jcou.2020.03.002.
- [45] C.S. Kalra, Y.I. Cho, A. Gutsol, A. Fridman, T.S. Rufael, Gliding arc in tornado using a reverse vortex flow, Rev. Sci. Instrum. 76 (2005) 025110, https://doi.org/ 10.1063/1.1854215.
- [46] A. Wu, J. Yan, H. Zhang, M. Zhang, C. Du, X. Li, Study of the dry methane reforming process using a rotating gliding arc reactor, Int. J. Hydrogen Energy 39 (2014) 17656–17670, https://doi.org/10.1016/j.ijhydene.2014.08.036.
- [47] H. Zhang, L. Li, X. Li, W. Wang, J. Yan, X. Tu, Warm plasma activation of CO2 in a rotating gliding arc discharge reactor, J. CO2 Util. 27 (2018) 472–479, https://doi.org/10.1016/j.jcou.2018.08.020.
- [48] N. Lu, D. Sun, Y. Xia, K. Shang, B. Wang, N. Jiang, J. Li, Y. Wu, Dry reforming of CH4-CO2 in AC rotating gliding are discharge: effect of electrode structure and gas parameters, Int. J. Hydrogen Energy 43 (2018) 13098–13109, https://doi. org/10.1016/j.ijhydene.2018.05.053.
- [49] F. Zhu, H. Zhang, X. Yan, J. Yan, M. Ni, X. Li, X. Tu, Plasma-catalytic reforming of CO2-rich biogas over Ni/γ-Al2O3 catalysts in a rotating gliding arc reactor, Fuel 199 (2017) 430–437, https://doi.org/10.1016/j.fuel.2017.02.082.
- [50] H. Zhang, C. Du, A. Wu, Z. Bo, J. Yan, X. Li, Rotating gliding arc assisted methane decomposition in nitrogen for hydrogen production, Int. J. Hydrogen Energy 39 (2014) 12620–12635, https://doi.org/10.1016/j.ijhydene.2014.06.047.
- [51] J.-L. Liu, H.-W. Park, W.-J. Chung, D.-W. Park, High-efficient conversion of CO2 in AC-pulsed tornado gliding arc plasma, Plasma Chem. Plasma Process. 36 (2016) 437–449, https://doi.org/10.1007/s11090-015-9649-2.
- [52] J.-L. Liu, H.-W. Park, W.-J. Chung, W.-S. Ahn, D.-W. Park, Simulated biogas oxidative reforming in AC-pulsed gliding arc discharge, Chem. Eng. J. 285 (2016) 243–251, https://doi.org/10.1016/j.cej.2015.09.100.
- [53] C.S. Kalra, A.F. Gutsol, A.A. Fridman, Gliding arc discharges as a source of intermediate plasma for methane partial oxidation, IEEE Trans. Plasma Sci. 33 (2005) 32–41, https://doi.org/10.1109/TPS.2004.842321.
- [54] T. Nınnally, K. Gutsol, A. Rabinovich, A. Fridman, A. Gutsol, A. Kemoun, Dissociation of CO2 in a low current gliding arc plasmatron, J. Phys. D Appl. Phys. 44 (2011) 274009, https://doi.org/10.1088/0022-3727/44/27/274009
- [55] S. Van Alphen, J. Slaets, S. Ceulemans, M. Aghaei, R. Snyders, A. Bogaerts, Effect of N2 on CO2-CH4 conversion in a gliding are plasmatron: can this major component in industrial emissions improve the energy efficiency? J. CO2 Util. 54 (2021) 101767 https://doi.org/10.1016/j.jcou.2021.101767.
- [56] M. Ramakers, S. Heijkers, T. Tytgat, S. Lenaerts, A. Bogaerts, Combining CO2 conversion and N2 fixation in a gliding arc plasmatron, J. CO2 Util. 33 (2019) 121–130, https://doi.org/10.1016/j.jcou.2019.05.015.
 [57] W. Xu, S. Van Alphen, V.V. Galvita, V. Meynen, A. Bogaerts, Effect of gas
- [57] W. Xu, S. Van Alphen, V.V. Galvita, V. Meynen, A. Bogaerts, Effect of gas composition on temperature and CO2 conversion in a gliding arc plasmatron reactor: insights for post-plasma catalysis from experiments and computation, ChemSusChem 17 (2024) e202400169, https://doi.org/10.1002/ cssc.202400169.
- [58] J. Slaets, M. Aghaei, S. Ceulemans, S. Van Alphen, A. Bogaerts, CO2 and CH4 conversion in "real" gas mixtures in a gliding arc plasmatron: how do N2 and O2 affect the performance? Green Chem. 22 (2020) 1366–1377, https://doi.org/10.1039/C9GC03743H
- [59] S. Kreuznacht, M. Purcel, S. Böddeker, P. Awakowicz, W. Xia, M. Muhler, M. Böke, A. von Keudell, Comparison of the performance of a microwave plasma torch and a gliding arc plasma for hydrogen production via methane pyrolysis, Plasma Process. Polym. 20 (2023) 2200132, https://doi.org/10.1002/ ppap.202200132.
- [60] R. Vertongen, A. Bogaerts, How important is reactor design for CO2 conversion in warm plasmas? J. CO2 Util. 72 (2023) 102510 https://doi.org/10.1016/j. icou 2023 102510
- [61] R. Bryssinck, G.J. Smith, C. O'Modhrain, T.R.C. Van Assche, G. Trenchev, A. Bogaerts, Performance of a gliding arc plasmatron pilot reactor with integrated carbon bed and recirculation for upscaled CO2 conversion, React. Chem. Eng. 10 (2025) 1910–1923, https://doi.org/10.1039/D5RE00190K.
- [62] F. Girard-Sahun, O. Biondo, G. Trenchev, G. van Rooij, A. Bogaerts, Carbon bed post-plasma to enhance the CO2 conversion and remove O2 from the product stream, Chem. Eng. J. 442 (2022) 136268, https://doi.org/10.1016/j. cei.2022.136268.
- [63] V. Vermeiren, A. Bogaerts, Plasma-based CO2 conversion: to quench or not to quench? J. Phys. Chem. C 124 (2020) 18401–18415, https://doi.org/10.1021/ acs.jpcc.0c04257.
- [64] A. Bogaerts, C. De Bie, R. Snoeckx, T. Kozák, Plasma based CO2 and CH4 conversion: a modeling perspective, Plasma Process. Polym. 14 (2017) 1600070, https://doi.org/10.1002/ppap.201600070.
- [65] J. Pacheco, G. Soria, M. Pacheco, R. Valdivia, F. Ramos, H. Frías, M. Durán, M. Hidalgo, Greenhouse gas treatment and H2 production, by warm plasma reforming, Int. J. Hydrogen Energy 40 (2015) 17165–17171, https://doi.org/ 10.1016/j.ijhydene.2015.08.062.
- [66] M. Albrechts, I. Tsonev, A. Bogaerts, Can post-plasma CH4 injection improve plasma-based dry reforming of methane? A modeling study, Green Chem. 26 (2024) 9712–9728, https://doi.org/10.1039/D4GC02889A.
- [67] C. Hyun Cho, J.H. Kim, J.K. Yang, I.S. Park, Y.-S. Choi, I.J. Kang, Dry reforming process using microwave plasma generator with high carbon dioxide conversion efficiency for syngas production, Fuel 361 (2024) 130707, https://doi.org/ 10.1016/j.fuel.2023.130707.

- [68] E.R. Mercer, M. Albrechts, R. De Meyer, I. Fedirchyk, E. Morais, S. Bals, A. Bogaerts, Dual injection in a CO2 microwave plasma: exploring post-plasma quenching with CH4 and comparison with DRM, Chem. Eng. J. 521 (2025) 166038, https://doi.org/10.1016/j.cej.2025.166038.
- [69] H. Kwon, T. Kim, S. Song, Dry reforming of methane in a rotating gliding arc plasma: improving efficiency and syngas cost by quenching product gas, J. CO2 Util. 70 (2023) 102448, https://doi.org/10.1016/j.jcou.2023.102448.
- [70] J. Martin-del-Campo, M. Uceda, S. Coulombe, J. Kopyscinski, Plasma-catalytic dry reforming of methane over Ni-supported catalysts in a rotating gliding arc – Spouted bed reactor, J. CO2 Util. 46 (2021) 101474, https://doi.org/10.1016/j. icou.2021.101474
- [71] Z.A. Allah, J.C. Whitehead, Plasma-catalytic dry reforming of methane in an atmospheric pressure AC gliding arc discharge, Catal. Today 256 (2015) 76–79, https://doi.org/10.1016/j.cattod.2015.03.040.
- [72] W. Xu, L.C. Buelens, V.V. Galvita, A. Bogaerts, V. Meynen, Improving the performance of gliding arc plasma-catalytic dry reforming via a new post-plasma tubular catalyst bed, J. CO2 Util. 83 (2024) 102820, https://doi.org/10.1016/j. jcou.2024.102820.
- [73] J.-L. Liu, Z. Li, J.-H. Liu, K. Li, H.-Y. Lian, X.-S. Li, X. Zhu, A.-M. Zhu, Warm-plasma catalytic reduction of CO2 with CH4, Catal. Today 330 (2019) 54–60, https://doi.org/10.1016/j.cattod.2018.05.046.
- [74] J. Slaets, E. Morais, A. Bogaerts, Afterglow quenching in plasma-based dry reforming of methane: a detailed analysis of the post-plasma chemistry via kinetic modelling, RSC Sustain. 3 (2025) 1477–1493, https://doi.org/10.1039/ DASIJ006786
- [75] O. Biondo, K. Wang, H. Zhang, A. Bogaerts, Coupling a CO2 plasma with a carbon bed: the closer the better, Chem. Eng. J. 507 (2025) 160190, https://doi.org/ 10.1016/j.cej.2025.160190.
- [76] C. O'Modhrain, Y. Gorbanev, A. Bogaerts, Post-plasma carbon bed design for CO2 conversion: does size and insulation matter? J. Energy Chem. 104 (2025) 312–323, https://doi.org/10.1016/j.jechem.2024.12.066.
- [77] R. Garcia-Villalva, M. Biset-Peiró, A. Alarcón, C. Bacariza, S. Murcia-López, J. Guilera, Comparison of methane reforming routes for hydrogen production using dielectric barrier discharge plasma-catalysis, Int. J. Hydrogen Energy 59 (2024) 1367–1375, https://doi.org/10.1016/j.ijhydene.2024.02.161.
- [78] D. Mei, B. Ashford, Y.-L. He, X. Tu, Plasma-catalytic reforming of biogas over supported Ni catalysts in a dielectric barrier discharge reactor: effect of catalyst supports, Plasma Process. Polym. 14 (2017) 1600076, https://doi.org/10.1002/ ppap.201600076.
- [79] J.A. Andersen, J.M. Christensen, M. Østberg, A. Bogaerts, A.D. Jensen, Plasma-catalytic dry reforming of methane: screening of catalytic materials in a coaxial packed-bed DBD reactor, Chem. Eng. J. 397 (2020) 125519, https://doi.org/10.1016/j.cej.2020.125519.
- [80] S.M. Chun, D.H. Shin, S.H. Ma, G.W. Yang, Y.C. Hong, CO2 microwave plasma—catalytic reactor for efficient reforming of methane to syngas, Catalysts 9 (2019), https://doi.org/10.3390/catal9030292.
- [81] J. Pan, T. Chen, Y. Gao, Y. Liu, S. Zhang, Y. Liu, T. Shao, Numerical modeling and mechanism investigation of nanosecond-pulsed DBD plasma-catalytic CH4 dry reforming, J. Phys. D Appl. Phys. 55 (2022), https://doi.org/10.1088/1361-6463/ac2ad8
- [82] A. Aziznia, H.R. Bozorgzadeh, N. Seyed-Matin, M. Baghalha, A. Mohamadalizadeh, Comparison of dry reforming of methane in low temperature hybrid plasma-catalytic corona with thermal catalytic reactor over Ni/γ-Al2O3, J. Nat. Gas Chem. 21 (2012) 466–475, https://doi.org/10.1016/ \$1003-9953(11)60392-7
- [83] X. Tu, J.C. Whitehead, Plasma-catalytic dry reforming of methane in an atmospheric dielectric barrier discharge: understanding the synergistic effect at low temperature, Appl. Catal. B Environ. 125 (2012) 439–448, https://doi.org/ 10.1016/j.apcatb.2012.06.006.
- [84] Q. Wang, B.-H. Yan, Y. Jin, Y. Cheng, Dry reforming of methane in a dielectric barrier discharge reactor with Ni/Al2O3 catalyst: interaction of catalyst and plasma, Energy Fuel 23 (2009) 4196–4201, https://doi.org/10.1021/ef900286j.
- [85] X. Gao, Z. Lin, T. Li, L. Huang, J. Zhang, S. Askari, N. Dewangan, A. Jangam, S. Kawi, Recent developments in dielectric barrier discharge plasma-assisted catalytic dry reforming of methane over Ni-based catalysts, Catalysts 11 (2021), https://doi.org/10.3390/catal11040455.
- [86] A.H. Khoja, M. Tahir, N.A.S. Amin, Evaluating the performance of a Ni catalyst supported on La2O3-MgAl2O4 for dry reforming of methane in a packed bed dielectric barrier discharge plasma reactor, Energy Fuel 33 (2019) 11630–11647, https://doi.org/10.1021/acs.energyfuels.9b02236.
- [87] J. Van Turnhout, D. Aceto, A. Travert, P. Bazin, F. Thibault-Starzyk, A. Bogaerts, F. Azzolina-Jury, Observation of surface species in plasma-catalytic dry reforming of methane in a novel atmospheric pressure dielectric barrier discharge in situ IR cell, Catal. Sci. Technol. 12 (2022) 6676–6686, https://doi.org/10.1039/D2CY00311B.
- [88] Y.X. Zeng, L. Wang, C.F. Wu, J.Q. Wang, B.X. Shen, X. Tu, Low temperature reforming of biogas over K-, Mg- and Ce-promoted Ni/Al2O3 catalysts for the production of hydrogen rich syngas: understanding the plasma-catalytic synergy, Appl. Catal. B Environ. 224 (2018) 469–478, https://doi.org/10.1016/j. apcatb.2017.10.017.
- [89] A.H. Khoja, M. Tahir, N.A.S. Amin, Recent developments in non-thermal catalytic DBD plasma reactor for dry reforming of methane, Energy Convers. Manag. 183 (2019) 529–560, https://doi.org/10.1016/j.enconman.2018.12.112.
- [90] J. Van Turnhout, K. Rouwenhorst, L. Lefferts, A. Bogaerts, Plasma catalysis: what is needed to create synergy? EES Catal. 3 (2025) 669–693, https://doi.org/ 10.1039/D5EY00027K.

- [91] B. Loenders, R. Michiels, A. Bogaerts, Is a catalyst always beneficial in plasma catalysis? Insights from the many physical and chemical interactions, J. Energy Chem. 85 (2023) 501–533, https://doi.org/10.1016/j.jechem.2023.06.016.
- [92] K. Li, J.-L. Liu, X.-S. Li, X. Zhu, A.-M. Zhu, Warm plasma catalytic reforming of biogas in a heat-insulated reactor: dramatic energy efficiency and catalyst autoreduction, Chem. Eng. J. 288 (2016) 671–679, https://doi.org/10.1016/j. cei.2015.12.036.
- [93] C. O'Modhrain, A. Pajares, E. Coutino-Gonzalez, Y. de Vos, P. Guardia, Y. Gorbanev, B. Michielsen, A. Bogaerts, Dry reforming of methane in gliding arc plasma: bridging thermal and post-plasma catalysis, EES Catal. (2025), https:// doi.org/10.1039/D5EY00067J.
- [94] I.A.W. Filot, Introduction to Microkinetic Modeling, Technische Universiteit Eindhoven, Eindhoven, 2022.
- [95] E.B. Sterk, A.-E. Nieuwelink, M. Monai, J.N. Louwen, E.T.C. Vogt;, I.A.W. Filot, B. M. Weckhuysen, Structure sensitivity of CO2 conversion over nickel metal nanoparticles explained by micro-kinetics simulations, JACS Au 2 (2022) 2714–2730, https://doi.org/10.1021/jacsau.2c00430.
- [96] J.K. Nørskov, F. Studt, F. Abild-Pedersen, T. Bligaard, Surface equilibria, in: Fundam. Concepts Heterog. Catal., 1st ed., John Wiley & Sons, Inc., 2014, pp. 26–46, 10.1002/9781118892114.ch3.
- [97] R. Michiels, Y. Engelmann, A. Bogaerts, Plasma catalysis for CO2 hydrogenation: unlocking new pathways toward CH3OH, J. Phys. Chem. C 124 (2020) 25859–25872, https://doi.org/10.1021/acs.jpcc.0c07632.
- [98] B. Loenders, Y. Engelmann, A. Bogaerts, Plasma-catalytic partial oxidation of methane on Pt(111): a microkinetic study on the role of different plasma species, J. Phys. Chem. C 125 (2021) 2966–2983, https://doi.org/10.1021/acs. jpcc.0c09849.
- [99] B. Hammer, L.B. Hansen, J.K. Nørskov, Improved adsorption energetics within density-functional theory using revised Perdew-Burke-Ernzerhof functionals, Phys. Rev. B 59 (1999) 7413–7421, https://doi.org/10.1103/PhysRevB.59.7413.
- [100] A. Hjorth Larsen, J. Jørgen Mortensen, J. Blomqvist, I.E. Castelli, R. Christensen, M. Dułak, J. Friis, M.N. Groves, B. Hammer, C. Hargus, E.D. Hermes, P. C. Jennings, P. Bjerre Jensen, J. Kermode, J.R. Kitchin, E. Leonhard Kolsbjerg, J. Kubal, K. Kaasbjerg, S. Lysgaard, J. Bergmann Maronsson, T. Maxson, T. Olsen, L. Pastewka, A. Peterson, C. Rostgaard, J. Schiøtz, O. Schiütt, M. Strange, K. S. Thygesen, T. Vegge, L. Vilhelmsen, M. Walter, Z. Zeng, K.W. Jacobsen, The atomic simulation environment—a Python library for working with atoms, J. Phys. Condens. Matter 29 (2017) 273002, https://doi.org/10.1088/1361-648X/aa680e.
- [101] M.C.J. Bradford, M.A. Vannice, Catalytic reforming of methane with carbon dioxide over nickel catalysts I. Catalyst characterization and activity, Appl. Catal. A. Gen. 142 (1996) 73–96. https://doi.org/10.1016/0926-860X(96)00065-8.
- [102] B. Rego de Vasconcelos, D. Pham Minh, E. Martins, A. Germeau, P. Sharrock, A. Nzihou, Highly-efficient hydroxyapatite-supported nickel catalysts for dry reforming of methane, Int. J. Hydrogen Energy 45 (2020) 18502–18518, https:// doi.org/10.1016/j.ijhydene.2019.08.068.
- [103] J.K. Nørskov, F. Studt, F. Abild-Pedersen, T. Bligaard, The potential energy diagram, in: Fundam. Concepts Heterog. Catal., Wiley, 2014, pp. 6–25, 10.1002/ 9781118892114.ch2.
- [104] O.V. Krylov, B.R. Shub, Nonequilibrium Processes in Catalysis, CRC Press, Boca Raton, 2018, 10.1201/9781351075022.
- [105] D.W. Blaylock, Y.-A. Zhu, W.H. Green, Computational investigation of the thermochemistry and kinetics of steam methane reforming over a multi-faceted nickel catalyst, Top. Catal. 54 (2011) 828, https://doi.org/10.1007/s11244-011-0704-7
- [106] K.H. Delgado, L. Maier, S. Tischer, A. Zellner, H. Stotz, O. Deutschmann, Surface reaction kinetics of steam- and CO2-reforming as well as oxidation of methane over nickel-based catalysts, Catalysts 5 (2015) 871–904, https://doi.org/ 10.3390/catal5020871.
- [107] S. Van Alphen, B. Wanten, F. Girard-Sahun, J. Slaets, J. Creel, M. Aghaei, A. Bogaerts, The role of CH4 in plasma-assisted CO2 and CH4 conversion in a

- rotating gliding arc plasma: insights revealed by experiments and modeling, ACS Sustain. Chem. Eng. 12 (2024) 15715–15728, https://doi.org/10.1021/acssuschemeng.4c06627.
- [108] R. Aerts, R. Snoeckx, A. Bogaerts, In-Situ chemical trapping of oxygen in the splitting of carbon dioxide by plasma, Plasma Process. Polym. 11 (2014) 985–992, https://doi.org/10.1002/ppap.201400091.
- [109] S. Van Alphen, H. Ahmadi Eshtehardi, C. O'Modhrain, J. Bogaerts, H. Van Poyer, J. Creel, M.-P. Delplancke, R. Snyders, A. Bogaerts, Effusion nozzle for energyefficient NOx production in a rotating gliding arc plasma reactor, Chem. Eng. J. 443 (2022), https://doi.org/10.1016/j.cej.2022.136529.
- [110] I. Tsonev, C. O'Modhrain, A. Bogaerts, Y. Gorbanev, Nitrogen fixation by an arc plasma at elevated pressure to increase the energy efficiency and production rate of NOx, ACS Sustain. Chem. Eng. 11 (2023) 1888–1897, https://doi.org/ 10.1021/acssuschemeng.2c06357.
- [111] B. Wanten, R. Vertongen, R. De Meyer, A. Bogaerts, Plasma-based CO2 conversion: how to correctly analyze the performance? J. Energy Chem. 86 (2023) 180–196, https://doi.org/10.1016/j.jechem.2023.07.005.
- [112] B. McBride, M. Zehe, S. Gordon, NASA Glenn coefficients for calculating thermodynamic properties of individual species, (2002).
- [113] O. Biondo, A. Hughes, A. van de Steeg, S. Maerivoet, B. Loenders, G. van Rooij, A. Bogaerts, Power concentration determined by thermodynamic properties in complex gas mixtures: the case of plasma-based dry reforming of methane, Plasma Sources Sci. Technol. 32 (2023) 045001, https://doi.org/10.1088/1361-6595/acc6ec.
- [114] S.-G. Wang, X.-Y. Liao, J. Hu, D.-B. Cao, Y.-W. Li, J. Wang, H. Jiao, Kinetic aspect of CO2 reforming of CH4 on Ni(111): a density functional theory calculation, Surf. Sci. 601 (2007) 1271–1284, https://doi.org/10.1016/j.susc.2006.12.059.
- [115] C. Vogt;, J. Kranenborg, M. Monai, B.M. Weckhuysen, Structure sensitivity in steam and dry methane reforming over nickel: activity and carbon formation, ACS Catal. 10 (2020) 1428–1438, https://doi.org/10.1021/acscatal.9b04193.
- [116] C. Fan, Y.-A. Zhu, M.-L. Yang, Z.-J. Sui, X.-G. Zhou, D. Chen, Density functional theory-assisted microkinetic analysis of methane dry reforming on Ni catalyst, Ind. Eng. Chem. Res. 54 (2015) 5901–5913, https://doi.org/10.1021/acs. iecr.5b00563.
- [117] T.P. Beebe Jr., D.W. Goodman, B.D. Kay, J.T. Yates Jr., Kinetics of the activated dissociative adsorption of methane on the low index planes of nickel single crystal surfaces, J. Chem. Phys. 87 (1987) 2305–2315, https://doi.org/10.1063/ 1.453162
- [118] F. Abild-Pedersen, O. Lytken, J. Engbæk, G. Nielsen, I. Chorkendorff, J. K. Nørskov, Methane activation on Ni(111): effects of poisons and step defects, Surf. Sci. 590 (2005) 127–137, https://doi.org/10.1016/j.susc.2005.05.057.
- [119] J.M. Ginsburg, J. Piña, T. El Solh, H.I. de Lasa, Coke Formation over a nickel catalyst under methane dry reforming conditions: thermodynamic and kinetic models, Ind. Eng. Chem. Res. 44 (2005) 4846–4854, https://doi.org/10.1021/ io0406333
- [120] A.S.A. Al-Fatish, A.A. Ibrahim, A.H. Fakeeha, M.A. Soliman, M.R.H. Siddiqui, A. E. Abasaeed, Coke formation during CO2 reforming of CH4 over alumina-supported nickel catalysts, Appl. Catal. A. Gen. 364 (2009) 150–155, https://doi.org/10.1016/j.apcata.2009.05.043.
- [121] M.K. Nikoo, N.A.S. Amin, Thermodynamic analysis of carbon dioxide reforming of methane in view of solid carbon formation, Fuel Process. Technol. 92 (2011) 678–691, https://doi.org/10.1016/j.fuproc.2010.11.027.
- [122] M. Kennema, P.A. Rowntree, The reactivity and initial carbonization of an Unsupported Nickel catalyst in dry reforming of methane, J. Power Sources 453 (2020) 226753, https://doi.org/10.1016/j.jpowsour.2019.226753.
- 123] C.T. Campbell, The degree of rate control: a powerful tool for catalysis research, ACS Catal. 7 (2017) 2770–2779, https://doi.org/10.1021/acscatal.7b00115.
- [124] J. Wei, E. Iglesia, Isotopic and kinetic assessment of the mechanism of reactions of CH4 with CO2 or H2O to form synthesis gas and carbon on nickel catalysts, J. Catal. 224 (2004) 370–383, https://doi.org/10.1016/j.jcat.2004.02.032.